

UNIVERSITY OF HAMBURG

BACHELOR'S THESIS

---

**van der Waals Corrections for Density  
Functional Theory**

**DFT+D2 applied to Graphene-hBN-Heterostructures**

---

*Author: Janosh Riebesell*

*Supervisor: Prof. Alexander  
Lichtenstein*

*A thesis submitted in fulfillment of the requirements  
for a Bachelor's degree*

*in the*

Group of Alexander Lichtenstein  
First Institute for Theoretical Physics at the University of Hamburg

September 2014

## Abstract

In recent initiatives aiming to develop materials for next-generation processors, graphene-based van der Waals heterostructures have emerged as one of the most promising candidates. It has been shown that interlayer binding in these two-dimensional crystal stacks is dominated by long-range molecular dispersion forces. This poses a challenge to popular (semi-)local approximations in the framework of density functional theory (DFT), requiring instead the use of highly expensive nonlocal approaches.

Here, we search for a computationally efficient method of modelling van der Waals heterostructures. We proceed by modifying DFT's conventional self-consistency cycle with Grimme et al.'s semiempirical dispersion correction scheme. To test this marriage, we assess its performance on the simple model system of G-hBN, a heterostructure consisting of single-layer graphene (G) bound to hexagonal boron nitride (hBN). We investigate a range of properties including equilibrium configurations, total energies as a function of interlayer separation, Young's moduli, and band gaps. Each of these features serves as a point of comparison for four different implementations of the DFT approach:

- Firstly, we deploy unaltered DFT in the form of a local density approximation (LDA) based on the Ceperley-Alder exchange-correlation functional, and the generalized-gradient approximation (GGA) based on the Perdew-Burke-Ernzerhof functional.
- In a second step, we add Grimme et al.'s dispersion correction and repeat all calculations.

Subsequently, results are compared among each other and with experiment wherever possible. Elsewhere, we fall back on theoretical findings obtained with highly accurate calculations in the nonlocal random phase approximation (RPA).

We report partial achievement of our initial goal with both LDA and modified GGA delivering realistic results in certain areas. We advise to refrain from using GGA and modified LDA on our specific test system of G-hBN as we have shown them to produce grossly under- and overestimated binding, respectively. We expect this behaviour to hold true also for other van der Waals heterostructures.

## Zusammenfassung

Aktuelle Initiativen zur Entwicklung von Materialien für Prozessoren der nächsten Generation zeigten, dass besonders graphenbasierte Heterostrukturen über großes Potential verfügen. Interplanare Bindungen zwischen diesen Schichten aus zweidimensionalen Kristallen konnten vor allem auf langreichweitige molekulare Dispersionskräfte zurückgeführt werden. Dies ist problematisch für (semi-)lokale Approximationen im Rahmen der Dichtefunktionaltheorie (DFT). Bisher erforderte die Modellierung langreichweitiger Dispersionskräfte teure, nicht-lokale Ansätze.

In dieser Arbeit suchen wir nach effizienten Methoden zur Modellierung von van der Waals Heterostrukturen. Unser Ansatz kombiniert konventionelle DFT mit semiempirischen Dispersionskorrekturen von Grimme et al. Wir testen die Leistungsfähigkeit dieser Verbindung anhand des simplen Modellsystems G-hBN bestehend aus einer Lage Graphen (G) gebunden an hexagonales Bornitrid (hBN). Wir bestimmen eine Reihe von Eigenschaften, unter anderem Gleichgewichtskonfigurationen, totale Energien als Funktion des interplanaren Abstands, Young's Moduli und Bandlücken. Jedes dieser Merkmale dient als Vergleichspunkt für vier verschiedene Implementationen des DFT-Ansatzes:

- Zunächst testen wir unveränderte DFT in Form von lokalen Dichtenäherungen (LDA) basierend auf dem Ceperley-Alder-Austauschkorrelationsfunktionals und die Gradientennäherung (GGA) basierend auf dem Perdew-Burke-Ernzerhof-Funktional.
- Im zweiten Schritt erweitern wir unser Modell um Grimme et al.'s Dispersionskorrektur und wiederholen alle Simulationen.

Anschließend werden Ergebnisse untereinander und mit experimentellen Daten verglichen, wo immer möglich. Andernfalls greifen wir auf theoretische Vorhersagen aus der präzisen, nicht-lokalen Random-Phase-Approximation (RPA) zurück.

Uns gelangen partielle Erfolge mit unserem Ansatz: Sowohl LDA als auch korrigiertes GGA liefern realistische Vorhersagen in einigen Testpunkten. Wir raten hingegen davon ab, GGA und korrigiertes LDA für Berechnungen unseres Testsystems G-hBN zu verwenden, da beide in unseren Untersuchungen Bindungsenergien massiv unter- bzw. überschätzten. Wir erwarten, dass unsere Befunde auch für andere van der Waals Heterostrukturen Bestand haben.

# Contents

<b>1</b>	<b>Introduction</b>	<b>5</b>
<b>2</b>	<b>Foundations of Density Functional Theory</b>	<b>7</b>
2.1	A short Recap of Quantum Mechanics . . . . .	7
2.2	The Hohenberg-Kohn theorem . . . . .	9
2.3	The Kohn-Sham Method . . . . .	10
2.4	Pseudopotentials and the Projector Augmented Wave Method . . . . .	15
2.5	The unknown Exchange-Correlation Functional . . . . .	16
2.5.1	Local Density Approximation . . . . .	17
2.5.2	Generalized-Gradient Approximation . . . . .	18
2.6	Grimme's van der Waals corrections . . . . .	19
<b>3</b>	<b>The Vienna Ab-Initio Simulation Package</b>	<b>22</b>
3.1	Operation . . . . .	22
<b>4</b>	<b>Graphene and hexagonal Boron Nitride</b>	<b>24</b>
<b>5</b>	<b>Results and Discussion</b>	<b>29</b>
5.1	Relaxation of Graphene on hexagonal Boron Nitride . . . . .	29
5.2	Total Energy Calculations . . . . .	30
5.2.1	LDA . . . . .	31
5.2.2	GGA . . . . .	31
5.2.3	LDA with Grimme's corrections . . . . .	32
5.2.4	GGA with Grimme's corrections . . . . .	33
5.3	Young's modulus . . . . .	34
5.3.1	LDA and GGA . . . . .	35
5.3.2	LDA and GGA with Grimme's corrections . . . . .	37
5.4	Band Structure and Band Gap . . . . .	38
5.4.1	LDA and GGA . . . . .	39
5.4.2	LDA and GGA with Grimme's corrections . . . . .	40
5.5	Method Comparison . . . . .	41
<b>6</b>	<b>Summary and Outlook</b>	<b>44</b>

# List of Figures

1.1	Total energy curves as predicted by different methods for a simple heterostructure of graphene on hBN . . . . .	5
2.1	Kohn-Sham self-consistency cycle . . . . .	14
2.2	Norm-conserving pseudopotential . . . . .	15
2.3	Some of the choices in density functional theory . . . . .	19
4.1	Hexagonal moiré structure consisting of many graphene and hBN unit cells . . . .	25
4.2	Moiré pattern for graphene on hBN with misaligned crystallographic axes . . . .	26
4.3	Six representatively chosen stacking configurations of graphene on hBN . . . . .	26
4.4	Moiré pattern of graphene-hBN . . . . .	27
4.5	Young's modulus distribution in graphene an hBN measured with an atomic force microscope . . . . .	27
5.1	Comparison of the total ground state energy per unit cell as a function of the interlayer spacing $d$ for six different stackings . . . . .	30
5.2	Comparison of the total ground state energy per unit cell as a function of the interlayer spacing $d$ for six different stackings. . . . .	32
5.3	Strain energy $E_{\text{str}}$ per unit cell as a function of strain in different areas of the moiré pattern . . . . .	35
5.4	Experimental AFM observations of moiré patterns and Young's modulus oscillations for graphene on hBN . . . . .	37
5.5	Strain energy $E_{\text{str}}$ per unit cell with Grimme's corrections as a function of strain in different areas of the moiré pattern . . . . .	37
5.6	Band structure along a path of high symmetry through the graphene-hBN Brillouin zone of configuration C5 in a relaxed state . . . . .	39
5.7	Band structure along a path of high symmetry through the graphene-hBN Brillouin zone of configuration C5 in a relaxed state . . . . .	41
5.8	Methodical comparison of LDA, GGA and RPA via total energies for C5 as a function of the interlayer distance $d$ . . . . .	42

# 1 Introduction

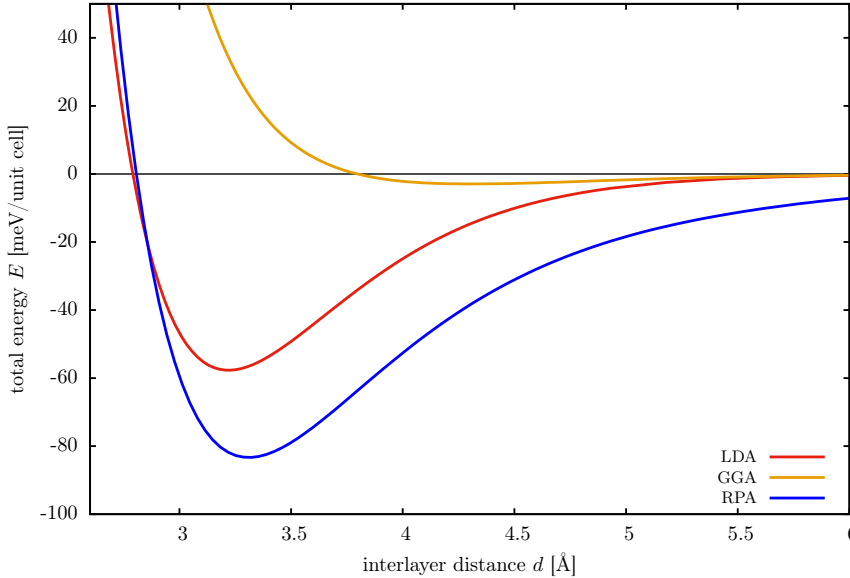


Figure 1.1: Total energy curves as predicted by different methods for GBN. RPA data was kindly provided by ref. [1].

The entire idea for what the topic of my thesis could be originated from a graph published in Physical Review by my academic advisor Burkhard Sachs in 2011 [1, p. 2]. A replicate of this graph is shown in fig. 1.1. The three curves each constitute a prediction for the total energy as a function of interlayer separation in a system made up of graphene fused with hBN. Although supposedly describing the same system, the curves differ considerably. That is because they originate from three different methods.

To understand which one we should expect to lie closest to reality, we will briefly explain the different concepts. The local density and generalized gradient approximations of density functional theory are quantum mechanical approaches which substitute a system’s wave function by its particle density as the primary container of information. This is a remarkable simplification. It replaces the complexity of a function depending for an  $n$ -particle system on  $3n$  spatial coordinates with a function of just three coordinates.<sup>1</sup> The total energy of a system is then split up into kinetic, interaction, correlation and exchange contributions and each of these is calculated as a functional of the density. The entire complexity of the problem is packed into the latter two parts. While the exchange energy can often be well approximated with an analytic expression derived from the homogeneous electron gas, the correlation energy may be obtained analytically only for the most basic systems. This is where the LDA and GGA come in, approximating the contribution from this term at every point in space based solely on the local particle density and, in the case of GGA, on its gradient. This is called a local approximation because strictly speaking, exchange and correlation energies are affected by the electron density of every corner of the system.

Their local nature is also the reason why for systems exhibiting a strong dependence on

<sup>1</sup>To illustrate just how inefficient a many-body wave-function is in uniquely determining a system’s state, consider this example: Imagine a real-space representation of  $\Psi$  on a mesh, in which each coordinate is discretized by using just 10 mesh points along its axes, which isn’t very much at all. For  $n$  electrons,  $\Psi$  becomes a function of  $3n$  coordinates, if we ignore spin and take  $\Psi$  to be real. Thus,  $10^{3n}$  values are required to fully determine  $\Psi$  on this mesh. The particle density  $\rho(\mathbf{r})$  is a function of three coordinates, and requires  $10^3$  values on the same mesh. For  $n = 10$  electrons, which again is not very much, the many-body wave function consequently requires  $10^{30}/10^3 = 10^{27}$  times more storage space than the density. Clever use of symmetries can reduce these ratios, but the full many-body wave function remains inaccessible for systems with more than a few electrons. [2, p. 1319]

long-range van der Waals interactions, such as our test system G-hBN, LDA and GGA fail to reproduce experimentally observed behavior. In contrast, the blue curve in fig. 1.1, delivered by RPA should be considered the closest representation of reality. Unlike LDA and GGA, RPA refrains from making any sort of local approximation to potentially significant long-range interactions. Unfortunately, this virtue is also its downfall, as it makes RPA incredibly expensive computationally, and, due to today's constraints in computation power, very restrictive on larger systems.

Theoretical solid state physics is therefore left with less than ideal tools. This poses a serious hurdle to continued effective research on van der Waals heterostructures. To establish an adequate backdrop for the following contents of this thesis, we will illustrate the dilemma a little more specifically here: The first-time isolation of graphene in 2004 [3] was followed by a period of intense scientific research revealing remarkable properties across the chart. Graphene conducted heat with astounding speed [4], it displayed extremely high charge carrier mobility [5] and boasted mechanical strength far superior to any material ever investigated before, enduring 100 times greater strain forces than steel [6]. It did not take scientists long to realize the huge potential graphene might offer a wide range of applications, among them new generations of nanoelectronics [7], particularly transistors with greatly improved clock speeds [8].

Unfortunately, further investigations into this matter exposed a fundamental problem. While graphene provides superior conductivity when compared to conventional silicon, it also features a vanishing intrinsic band gap. This makes it much harder to externally manipulate its state of conductance. To construct a functioning transistor, however, requires the ability to induce a so-called pinch-off state where carrier transport is severely hindered or even halted completely. Subsequently, it was experimented if adhesion of graphene to a range of materials could improve pinch-off characteristics [9]. Compounds consisting of graphene adhered to a hexagonal boron nitride substrate were shown to introduce an intrinsic band gap into graphene low-energy  $p_z$  states [1, 7, 9, 10], making them perhaps the most promising solution to this issue. However, to make further progress in this area, theory required an appropriate tool for modelling such systems. As explained above, this proved difficult for the common workhorse in this field, DFT, which failed to correctly reproduce structural and mechanical data measured experimentally. The reason being that these properties in van der Waals heterostructures resulted, of course, to a large extent from van der Waals interactions not taken into account by DFT. The alternatives were nonlocal methods such as the RPA, which produced great results when applied to very small systems but were simply too prohibitively expensive for large model calculations.

Here, we see an opportunity for improvement. In an attempt to solve this problem, we set out to investigate, whether DFT's inherent inability to model van der Waals interactions might be curable. To that end, we tested a very simple, semiempirical correction scheme for long-range molecular dispersion forces developed by Stefan Grimme and colleagues [11]. Our choice fell on this option for obvious reasons. Firstly, it was specifically designed as an add-on to the very versatile foundation of density functional theory, which is capable of efficiently modelling large interacting many-body systems. Secondly, it is a simple sum over pairwise forces that contributes only negligibly to the total computation cost of a regular DFT calculation. It therefore creates no additional constraints on the model system's size.

Before presenting and then evaluating our results in chapters 5 and 6, we will cover some of the technicalities of density functional theory, introduce the materials involved, and describe the software used in the following three chapters.

# 2 | Foundations of Density Functional Theory

Modern solid state physics is devoted to the study of rigid matter in all its appearances, covering exciting current research topics such as high-temperature superconductivity, strongly correlated materials, two dimensional and quasicrystals, and van der Waals heterostructures. Partly due to the significance these topics hold for solving modern-day challenges such as worldwide energy distribution and further advancement of transistor technology, solid state physics has grown to become one of the largest and most successful branches of condensed matter physics. It is generally concerned with researching the following properties of newly discovered materials:

- crystal structure
- mechanical stability
- phonon scattering
- density and atomic composition of defects
- band structure and density of states
- electrical and heat conduction

Among them, these characteristics contain central know how for bringing new materials to real-world applications. To learn more about a new system, it is generally necessary to tackle the problem on a quantum mechanical level, ideally by solving the system's Schrödinger equation. Expectably, the time and effort involved in such a calculation scales exponentially with a system's complexity, something often referred to as the computational barrier. Even after incorporating possible symmetries and simplifying approximations, using the Schrödinger equation to solve systems consisting of more than 10 particles is not feasible with today's technology. As this number is unlikely to increase substantially in the foreseeable future, physicists have come up with a number of sophisticated methods to tackle such and even larger systems. One very common approach is density functional theory. It proved especially useful when trying to determine the electronic structure of a given solid state compound, making it the methodical framework of choice for this thesis. DFT therefore deserves to be covered in some detail in the following sections. The didactical introduction they provide is guided mainly by the very good summary of DFT from Klaus Capelle (ref. [2]) with occasional bits and pieces from other literature and publications, where indicated.

## 2.1 A short Recap of Quantum Mechanics

To get an idea of the inner workings of DFT, it is helpful to recall some of the fundamentals of quantum mechanics first: The state of a physical system at any given time  $t$  is determined by specifying its complex state vector  $|\Psi(t)\rangle$ , often referred to as wave function. All state vectors reside in a state space  $\mathcal{H}$  associated with this system. Mathematically,  $\mathcal{H}$  is a complex separable Hilbert space with an inner product. Its precise nature depends on the type of system; for instance, the state space of position and momentum states is the space of square-integrable functions. In such a Hilbert space, all vectors that differ only by a complex constant  $0 \neq c \in \mathbb{C}$  are said to represent the same state. Combined, these last statements form the first postulate of the Koppenhagener interpretation of quantum mechanics as developed by Paul Dirac, David Hilbert, John von Neumann, and others [12–15].

A fundamental way to obtain wave functions is to find solutions to a system's non-relativistic time-dependent Schrödinger equation

$$\frac{\partial}{\partial t}|\Psi(t)\rangle = \frac{1}{i\hbar}\hat{H}|\Psi(t)\rangle, \quad \left(\hat{H}|\Psi\rangle = E|\Psi\rangle\right), \quad (2.1)$$

where  $\hat{H}$  denotes the Hamilton operator and  $E$  the corresponding observable, i.e. the total energy. The time-independent Schrödinger equation shown in parentheses presents a considerable simplification. In solid state physics, it is often justified to solve this equation rather than eq. (2.1), particularly when a system is governed by time-independent atomic and molecular interactions. Equation (2.1) is a partial differential equation due to the first-order derivative with respect to time and the Hamilton operator containing second order derivatives with respect to position.<sup>1</sup> For the simple system of a single electron of mass  $m_e$  moving through a potential  $\hat{V}(\mathbf{r})$ , it takes the form

$$\hat{H}(\mathbf{r}) = \frac{\hat{\mathbf{p}}^2}{2m_e} + \hat{V}(\mathbf{r}) = -\frac{\hbar^2}{2m_e} \Delta_{\mathbf{r}} + \hat{V}(\mathbf{r}), \quad (2.2)$$

where  $\hat{\mathbf{p}} = -i\hbar\nabla$  is the momentum operator in position representation.

This thesis is concerned exclusively with the study of quantum mechanical many-body systems made up of electrons and atomic nuclei and the resulting implications for solids or, more precisely, stackings of two-dimensional crystals. In the process, the presence of nuclear matter, i.e. the crystal lattice is taken into account only in the form of a potential  $\hat{V}(\mathbf{r})$  acting on the electrons. The resulting  $n$ -electron Hamilton operator for this approach reads

$$\begin{aligned} \hat{H}_e &= \hat{T}_e + \hat{V}_{ee} + \hat{V}_{eI} \\ &= -\sum_{j=1}^n \frac{\hbar^2}{2m_e} \Delta_{\mathbf{r}_j} + \sum_{j>k}^n \frac{e^2}{4\pi\epsilon} \frac{1}{|\mathbf{r}_j - \mathbf{r}_k|} + \sum_{j=1}^n v_{e,jI}(\mathbf{r}_j). \end{aligned} \quad (2.3)$$

Here, lower case indices indicate electrons and upper case indices lattice ions. The operator  $\hat{T}_e$  stands for the electron kinetic energy, in which  $j$  sums over all  $n$  individual electrons.  $\hat{V}_{ee}$  is the electron-electron repulsion energy, and  $\hat{V}_{eI}$  is the electron-ion attraction (or repulsion) energy where

$$v_{e,jI}(\mathbf{r}_j) = -\sum_{J=1}^N \frac{Z_J e^2}{4\pi\epsilon} \frac{1}{|\mathbf{r}_j - \mathbf{r}_J|} \quad (2.4)$$

is the Coulomb interaction energy of electron  $j$  with all  $N$  ions [16, p. 3]. In both eqs. (2.3) and (2.4),  $\epsilon$  denotes the absolute dielectric permittivity of the given solid. One can see that in the scenario described by eq. (2.3),  $\hat{V}(\mathbf{r})$  takes the form of  $\hat{V}_{eI}$  as it is the only term in eq. (2.3) allowing for the existence of other matter besides the electrons.  $\hat{H}$  as written in eq. (2.3) is not exact in the sense that when applied to a system's wave function, it will not yield the correct total energy. This is because factoring in the lattice ions only as an electronic potential is not strictly accurate. It can be shown that eq. (2.3) should still deliver good results for real world systems. It is the *Born-Oppenheimer approximation* (BOA) to the still not exact but more sophisticated many-body Hamiltonian of a system of  $n$  electrons and  $N$  ions interacting solely via mutual Coulomb forces

$$\hat{H} = \hat{T}_e + \hat{V}_{ee} + \hat{V}_{eI} + \hat{T}_A + \hat{V}_{II}. \quad (2.5)$$

The two new terms  $\hat{T}_A$  and  $\hat{V}_{II}$  in this Hamiltonian reflect the atomic kinetic energy and the ion-ion interaction energy respectively. They are given by [16, p. 3]

$$\hat{T}_A = -\sum_{J=1}^N \frac{\hbar^2}{2m_J} \Delta_{\mathbf{r}_J} \quad \text{and} \quad \hat{V}_{II} = \sum_{J>K}^N \frac{Z_J Z_K e^2}{4\pi\epsilon} \frac{1}{|\mathbf{r}_J - \mathbf{r}_K|}. \quad (2.6)$$

The BOA draws its validity from the fact that in an arbitrary crystal, all atomic masses  $m_J, J \in \{1, \dots, N\}$  are at least three orders of magnitude larger than the electron mass  $m_e$ . As

<sup>1</sup>This inequality in the order of derivatives is testimony to the non-relativistic nature of eq. (2.1).

a consequence, the energy contribution  $\hat{T}_A \propto 1/m_J$  from the ionic kinetic energy is very small compared to the electronic kinetic energy. Essentially, the BOA performs the limit  $m_J \rightarrow \infty$ , thereby omitting the term  $\hat{T}_A$  entirely. From this approximation follows a system where all ionic motion is assumed to halt. Consequently, the ion-ion interaction energy  $\hat{V}_{II}$  can no longer change over time as the relative distances  $|\mathbf{r}_J - \mathbf{r}_K|$  between ions are fixed. This means that  $\hat{V}_{II}$  becomes just an added constant. We can safely omit it as well, since it effectively represents merely a shift to the system's zero-point energy. We are not accounting for gravity here, so the zero-point energy carries no meaning for us in the first place. Thus, the systematic error that stems from choosing the simpler Hamiltonian eq. (2.3) over eq. (2.5) is insignificant compared to the advantage of substantially reduced computation time.

With this brush-up of quantum mechanics in mind, we can move on to address some of the corner stones of DFT, namely the Hohenberg-Kohn theorem, the Kohn-Sham method, and the plane wave basis set in the following sections of this chapter.

## 2.2 The Hohenberg-Kohn theorem

The Hohenberg-Kohn theorem forms the centerpiece of density functional theory. It was contrived by Pierre Hohenberg and Walter Kohn at the University of Paris and published in a groundbreaking paper dated back as far as 1964 [17]. In this paper, Hohenberg and Kohn proved the applicability of exact density functional theory to any system of  $n$  interacting particles in an external potential  $\hat{V}_{\text{ext}}(\mathbf{r})$  [7, p. 6] (produced for example by fixed lattice ions). The theorem consists of two statements.

The first proves the existence of a definite mapping between the ground state particle density and the ground state total wave function and may be worded along the following lines:

**HK I** For any system of interacting particles in an external potential  $\hat{V}_{\text{ext}}(\mathbf{r})$ , the potential is determined uniquely, except for a constant, by the ground state particle density  $\rho_0(\mathbf{r})$  [18, p. 122].<sup>2</sup> Since, in turn,  $\hat{V}_{\text{ext}}(\mathbf{r})$  fixes the Hamiltonian  $\hat{H}$  we see that the full many-particle non-degenerate ground state  $\Psi_0(\mathbf{r}_1, \dots, \mathbf{r}_n)$  is a unique functional of  $\rho_0(\mathbf{r})$  [17, p. 865].

This implies that, given a *ground state* density  $\rho_0(\mathbf{r})$ , it is principally possible to calculate the corresponding ground state wave function  $\Psi_0(\mathbf{r}_1, \dots, \mathbf{r}_n)$  and from this in turn an arbitrary ground state observable  $\mathcal{O}_0$  [2, p. 1321] via

$$\mathcal{O}_0[\rho_0] = \langle \hat{\mathcal{O}}_0[\rho_0] \rangle = \left\langle \Psi_0[\rho_0] \left| \hat{\mathcal{O}}_0 \right| \Psi_0[\rho_0] \right\rangle. \quad (2.7)$$

Consequently, all ground state observables in a many-body system are functionals of  $\rho_0(\mathbf{r})$ . This is where density functional theory derived its name.

It may initially seem strange that  $\Psi_0(\mathbf{r}_1, \dots, \mathbf{r}_n)$  and  $\rho_0(\mathbf{r})$  are equally suited to characterize a system. How can a function of  $3n$  variables be calculated from a function with just 3 variables? It certainly works the other way round (the particle density may easily be calculated from the total wave function<sup>3</sup>), which would mean that both functions are equivalent. The reason this

<sup>2</sup>In other words, potentials differing only by a constant  $\Delta V \in \mathbb{R}$  lead to the same density  $\rho_0(\mathbf{r})$ .

<sup>3</sup>This can be done via the expectation value of the single-particle density operator  $\hat{\rho}(\mathbf{r}) = \sum_{i=1}^n \delta(\mathbf{r} - \mathbf{r}_i)$  with respect to the  $n$ -body wavefunction  $\Psi(\mathbf{r}_1, \dots, \mathbf{r}_n)$ :

$$\begin{aligned} \rho(\mathbf{r}) &= \langle \Psi | \hat{\rho}(\mathbf{r}) | \Psi \rangle = \sum_{i=1}^n \int \dots \int \delta(\mathbf{r} - \mathbf{r}_i) |\Psi(\mathbf{r}_1, \dots, \mathbf{r}_n)|^2 d^3 r_1 \dots d^3 r_n \\ &= n \int \dots \int |\Psi(\mathbf{r}, \mathbf{r}_2, \dots, \mathbf{r}_n)|^2 d^3 r_2 \dots d^3 r_n. \end{aligned} \quad (2.8)$$

works is due to implicit conditions imposed on the ground state wave function  $\Psi_0(\mathbf{r}_1, \dots, \mathbf{r}_n)$ . In addition to reproducing the ground state density, it needs to minimize the total energy  $E_{\hat{V}}[\rho_0]$  for a system with potential  $\hat{V}(\mathbf{r})$ :

$$E_{0,\hat{V}}[\rho_0] = \min \left\{ \langle \Psi_0 | \hat{H}_{\hat{V}} | \Psi_0 \rangle \mid \Psi_0 \text{ produces } \rho_0(\mathbf{r}) \right\}. \quad (2.9)$$

Here, the Hamiltonian  $\hat{H}_{\hat{V}}$  is of the kind specified in eq. (2.3) and the laxly phrased condition “produces” means that  $\Psi_0(\mathbf{r}_1, \dots, \mathbf{r}_n)$  has to fulfill eq. (2.8).

This also serves to explain why density functional theory can only be applied to the study of ground states. The implicit condition in eq. (2.9) does not pertain for energetically excited states.

The second statement says that the ground state particle density always minimizes the total energy:

**HK II** A *universal* functional for the energy  $E[\rho]$  in terms of the density  $\rho(\mathbf{r})$  can be defined, valid for any external potential  $\hat{V}_{\text{ext}}(\mathbf{r})$ . For any particular  $\hat{V}(\mathbf{r})$ , the exact ground state energy of the system is the global minimum value of this functional and the density  $\rho(\mathbf{r})$  that minimizes the functional is the exact ground state density  $\rho_0(\mathbf{r})$  [18].

To put this in context, **HK II** justifies the use of the variational principle on the ground state density. It means that for differentiable  $E[\rho]$ ,  $\rho_0(\mathbf{r})$  fulfills [7, p. 7]

$$\delta \left[ E[\rho] - \mu \left( \int \rho(\mathbf{r}) \, d^3r - n \right) \right] \Big|_{\rho=\rho_0} = 0, \quad (2.10)$$

which in turn yields the Euler-Lagrange equation for a system of  $n$  interacting particles

$$\mu = \frac{\delta E[\rho]}{\delta \rho} = v_{\text{ext}}(\mathbf{r}) + \frac{\delta F[\rho]}{\delta \rho}. \quad (2.11)$$

In eqs. (2.10) and (2.11),  $\mu$  is the chemical potential,  $v_{\text{ext}}(\mathbf{r}) = \delta V_{\text{ext}}(\mathbf{r})/\delta \rho$ , and  $F[\rho] = T[\rho] + V[\rho]$  is the sum of kinetic and Coulomb interaction energy for the  $n$ -particle system.  $F[\rho]$  is often referred to as the *universal* functional of  $\rho(\mathbf{r})$  because it is that part of the Hamiltonian in eq. (2.3) which is independent of the external potential  $V_{\text{ext}}(\mathbf{r})$ . As a reminder, in density functional theory  $V_{\text{ext}}(\mathbf{r})$  serves as the only quantity that uniquely identifies a system. At this point it should also be remarked that eq. (2.10) is still exact as long as  $F[\rho]$  is, and it applies to all systems which can be formulated by a Hamiltonian of the form 2.3.

To summarize this section, the power of the Hohenberg-Kohn theorem lies in the justification it provides for substituting a system’s wave function by its particle density as quantum mechanics’ primary container of information. It allows the calculation of observables by finding the particle density  $\rho_0(\mathbf{r})$ , a function of exactly three coordinates as opposed to having to solve an inseparable Schrödinger equation to obtain the total wave function  $\Psi(\mathbf{r}_1, \mathbf{r}_2, \dots, \mathbf{r}_n)$  dependent on  $3n$  coordinates. This on its own is a considerable simplification. Furthermore, it puts the powerful machinery of variational calculus at our disposal. The next section will deal with a game-changing technique introduced by Kohn and Sham that brings this huge theoretical potential much closer to real world use.

## 2.3 The Kohn-Sham Method

The Hohenberg-Kohn theorem has been mostly abstract considerations. Thus, let us assume a more concrete example, i.e. a system of  $n$  electrons specified by an explicitly stated external

potential  $v_{\text{ext}}(\mathbf{r})$ . Furthermore, we might assume to have reliably working approximations to both parts of the universal functional, namely  $T_e[\rho]$  and  $V_{ee}[\rho]$ . In principle, all one has to do then is to minimize the sum of kinetic, interaction and potential energy [2, p. 1323],

$$\begin{aligned} E_{V_{\text{ext}}}[\rho] &= T_e[\rho] + V_{ee}[\rho] + V_{eI}[\rho] \\ &= T_e[\rho] + V_{ee}[\rho] + \int \rho(\mathbf{r}') V_{\text{ext}}(\mathbf{r}') d^3r', \end{aligned} \quad (2.12)$$

with respect to the particle density. Whichever  $\rho(\mathbf{r})$  produces the lowest total energy will be the ground state particle density  $\rho_0(\mathbf{r})$ . The same counts for all parameters that have an effect on the external potential. In our case, this might be the lattice constant  $a$ . Then, via the particle density the total energy will also depend on this parameter, i.e.  $E_{V_{\text{ext}}}(a)$ . One can then determine both the ground state lattice constant and energy by finding the value  $a_0$  that minimizes  $E_{V_{\text{ext}}}(a)$ .<sup>4</sup> A variety of different quantities can be obtained in such a manner, for example intermolecular distances, bond angles, unit cell volumes, and even charge distributions. By further making use of the Hellman-Feynman theorem, we can calculate forces acting on the atoms creating the external potential from the derivative of the total energy with respect to the ionic coordinates [19]. All this follows from DFT without having to solve the many-body Schrödinger equation and without having to make a single-particle approximation [2, p. 1324]. In theory it should be possible to calculate all observables, since the Hohenberg-Kohn theorem guarantees that they are all functionals of  $\rho(\mathbf{r})$ . In practice, no one knows exactly how to do this. Another problem is that the minimization of  $E_{V_{\text{ext}}}[\rho]$  is, in general, a tough numerical problem all on its own. Moreover, one needs reliable approximations for  $T_e[\rho]$  and  $V_{ee}[\rho]$  [2, p. 1324]. A widely used method for solving these problems are the Kohn-Sham equations which we will introduce in this section.

In 1965, Kohn and Sham developed a scheme to perform the energy minimization indirectly. Research in this area was spurred by the fact that the minimization of an explicit energy functional of the particle density is almost never the most efficient undertaking. Instead, Kohn and Sham proposed not to work exclusively with the particle density but to replace it partially with a certain type of wave function: single-particle orbitals. We will see that this brings the appearance of a single-particle theory to DFT. Of course, the effects of an underlying many-body system will still be integrated by so-called exchange correlation functionals [20].

The first step is to decompose the kinetic energy functional  $T_e[\rho]$  (of the interacting electrons) into two parts

$$T_e[\rho] = T_{e,s}[\rho] + T_{e,c}[\rho], \quad (2.13)$$

- where  $T_{e,s}[\rho]$  represents the kinetic energy but without any interaction between particles and
- $T_{e,c}[\rho]$  picks up all the remainder [2, p. 1328].

The subscripts  $s$  and  $c$  stand for “single-particle” and “correlation”, respectively. An exact expression for the single-particle kinetic energy  $T_{e,s}[\rho]$  as a density functional is not known.<sup>5</sup> It can, however, be written in terms of the single-particle orbitals  $\phi_i(\mathbf{r}_i)$ ,  $i \in \{1, \dots, n\}$ , of the non-interacting system with density  $\rho(\mathbf{r})$  as follows

$$T_{e,s}[\phi_i] = -\frac{\hbar^2}{2m} \sum_{i=1}^n \int \phi_i^*(\mathbf{r}_i) \nabla^2 \phi_i(\mathbf{r}_i) d^3r_i, \quad (2.14)$$

<sup>4</sup>This requires all other parameters to be in their ground state configurations. Otherwise, simultaneous variations of all these parameters have to be taken into account, i.e. the whole parameter space has to be searched for the lowest total energy.

<sup>5</sup> $T_{e,s}[\rho]$  can be approximated in the local density approximation (see section 2.5.1) which leads back to an older theory, called the Thomas-Fermi model. It served as a precursor to modern density functional theory, developed independently by Llewellyn Thomas and Enrico Fermi in 1927. The Thomas-Fermi model yields poor quantitative predictions for real-world systems. Its age notwithstanding, the Thomas-Fermi kinetic energy functional is still occasionally used these days in alongside more sophisticated density approximations.

as it is simply the sum of the individual kinetic energies. In eq. (2.14),  $T_{e,s}[\phi_i]$  is an explicit orbital functional but only implicitly a functional of the density, that is  $T_{e,s}[\phi_i] = T_{e,s}[\phi_i\{\rho\}]$ , because all  $\phi_i(\mathbf{r}_i)$  depend on  $\rho(\mathbf{r})$ . The (formally exact) total energy eq. (2.12) functional can then be rewritten as

$$E_{V_{\text{ext}}}[\rho] = T_{e,s}[\phi_i\{\rho\}] + V_{ee,H}[\rho] + E_{xc}[\rho] + V_{eI}[\rho], \quad (2.15)$$

where  $V_{ee,H}[\rho]$  denotes the Hartree energy and serves to approximate the particle interactions

$$V_{ee}[\rho] \approx V_{ee,H}[\rho] = \frac{1}{2} \frac{e^2}{4\pi\epsilon} \iint \frac{\rho(\mathbf{r})\rho(\mathbf{r}')}{|\mathbf{r} - \mathbf{r}'|} d^3r d^3r', \quad (2.16)$$

and the functional  $E_{xc}[\rho]$  is called the *exchange-correlation* energy. By definition it absorbs the two sources of inaccuracy  $T_e[\phi_i\{\rho\}] \neq T_{e,s}[\phi_i\{\rho\}]$  and  $V_{ee}[\rho] \neq V_{ee,H}[\rho]$ . Thus

$$E_{xc}[\rho] = \underbrace{T_e[\rho] - T_{e,s}[\rho]}_{T_{e,c}[\rho]} + V_{ee}[\rho] - V_{ee,H}[\rho]. \quad (2.17)$$

Equation (2.15) is only formally exact, because the exchange-correlation energy is, of course, unknown. To break this problem down into smaller pieces, the latter is often subdivided into  $E_{xc}[\rho] = E_x[\rho] + E_c[\rho]$ , where  $E_x[\rho]$  is the exchange energy stemming from the Pauli principle and  $E_c[\rho]$  denotes the correlation energy which contains energetic contributions from interaction otherwise neglected in eq. (2.15). More specifically, it can be understood by recalling that the Hartree energy is obtained from an approximation of a many-body wave function  $\Psi(\mathbf{r}_1, \dots, \mathbf{r}_n)$  as an antisymmetrized product of single-particle orbitals  $\phi_i(\mathbf{r}_i)$  (Slater determinant) [2, p. 1324]. In this context, the correlation energy is defined as the difference between the full ground-state energy (obtained with the correct many-body wave function) and the one obtained from the Slater determinant. Back to the exchange energy, it can be stated explicitly when again resorting to the single-particle orbitals

$$E_x[\phi_i(\mathbf{r}_i)] = -\frac{1}{2} \frac{e^2}{4\pi\epsilon} \sum_{j,k} \iint \frac{\phi_j^*(\mathbf{r})\phi_k^*(\mathbf{r}')\phi_j(\mathbf{r}')\phi_k(\mathbf{r})}{|\mathbf{r} - \mathbf{r}'|} d^3r d^3r'. \quad (2.18)$$

Equation (2.18) is referred to as the Fock term and it is an essential ingredient to the Kohn-Sham method. Unfortunately, the correlation energy is not so easily dispatched, neither in density nor in orbital notation. An explicit expression can be found for a small number of systems, but none is known that could be called generally applicable, so it will be skipped for now.<sup>6</sup> Instead, we will finally come to the Kohn-Sham scheme of minimizing the total energy using the variational principle. Since  $T_{e,s}[\phi_i\{\rho\}]$  in eq. (2.15) is written explicitly as an orbital functional, it becomes clear why the minimization with respect to  $\rho(\mathbf{r})$  has to be done indirectly,

$$\begin{aligned} 0 &= \frac{\delta E_{V_{\text{ext}}}[\rho]}{\delta \rho(\mathbf{r})} = \frac{\delta T_{e,s}[\phi_i\{\rho\}]}{\delta \rho(\mathbf{r})} + \frac{\delta V_{ee,H}[\rho]}{\delta \rho(\mathbf{r})} + \frac{\delta E_{xc}[\rho]}{\delta \rho(\mathbf{r})} + \frac{\delta V_{eI}[\rho]}{\delta \rho(\mathbf{r})} \\ &= \frac{\delta T_{e,s}[\phi_i\{\rho\}]}{\delta \rho(\mathbf{r})} + v_H(\mathbf{r}) + v_{xc}(\mathbf{r}) + v_{\text{ext}}(\mathbf{r}). \end{aligned} \quad (2.19)$$

Here, the variation of the Hartree  $V_{ee,H}[\rho]$  energy with respect to the density yields the Hartree potential

$$v_H(\mathbf{r}) = \int \rho(\mathbf{r}') V_{\text{ext}}(\mathbf{r}') d^3r'. \quad (2.20)$$

<sup>6</sup>We will come back to this in sections 2.5.1 and 2.5.2 when discussing local approximations to the correlation energy.

The term  $v_{xc}(\mathbf{r}) = \delta E_{xc}[\rho]/\delta\rho(\mathbf{r})$  replacing the variation of the exchange correlation energy is called the exchange-correlation potential. At this point however, it is really just an empty definition, because neither  $v_{xc}(\mathbf{r})$  nor  $E_{xc}[\rho]$  can be expressed or calculated until a specific approximation has been chosen. The variation of  $V_{el}[\rho]$  simply results in the external potential acting on all particles. The critical step is to consider eq. (2.19) for a system of non-interacting particles. In this case, the minimization condition reads

$$0 = \frac{\delta E_{V_{\text{ext},s}}[\rho]}{\delta\rho(\mathbf{r})} = \frac{\delta T_{e,s}[\phi_i\{\rho\}]}{\delta\rho(\mathbf{r})} + \frac{\delta V_{eI,s}[\rho]}{\delta\rho(\mathbf{r})} = \frac{\delta T_{e,s}[\phi_i\{\rho\}]}{\delta\rho(\mathbf{r})} + v_{\text{ext},s}(\mathbf{r}), \quad (2.21)$$

since there is no Hartree potential and no exchange or correlation in a one particle system that lacks any sort of interaction [2, p. 1330]. Let's say the condition eq. (2.21) is satisfied by the single-particle density  $\rho_s(\mathbf{r})$ . If we then compare eq. (2.21) with the same condition but for a many-body system, i.e. eq. (2.19), it becomes clear that  $\rho_s(\mathbf{r})$  also solves the many-body condition if we set

$$v_{\text{ext},s}(\mathbf{r}) = v_H(\mathbf{r}) + v_{xc}(\mathbf{r}) + v_{\text{ext}}(\mathbf{r}). \quad (2.22)$$

This is remarkable as it means that we can calculate the particle density for a complex many-body system in a potential  $v_{\text{ext}}(\mathbf{r})$  by solving the Schrödinger equation of a non-interacting single-particle system with the so-called *Kohn-Sham potential*  $v_{\text{ext},s}(\mathbf{r})$  for each particle in turn, one at a time. Specifically, instead of having to solve a Schrödinger equation of the form

$$\left( -\sum_{j=1}^n \frac{\hbar^2}{2m_e} \Delta_{\mathbf{r}_j} + \sum_{j>k}^n \frac{e^2}{4\pi\epsilon} \frac{1}{|\mathbf{r}_j - \mathbf{r}_k|} + \sum_{j=1}^n v_{e_j I}(\mathbf{r}_j) \right) \Psi(\mathbf{r}_1, \dots, \mathbf{r}_n) = E \Psi(\mathbf{r}_1, \dots, \mathbf{r}_n), \quad (2.23)$$

which is practically impossible for  $n > 10$ , it is sufficient to solve  $n$  Schrödinger equations of the form

$$\left( -\frac{\hbar^2}{2m_e} \Delta_{\mathbf{r}_i} + v_{\text{ext},s}(\mathbf{r}_i) \right) \phi_i(\mathbf{r}_i) = E_i \phi_i(\mathbf{r}_i) \quad (2.24)$$

Equation (2.24) produces single-particle orbitals that when combined recreate the particle density  $\rho(\mathbf{r})$  of the original many-body system. The combination is done by summing up all single-particle probability distributions multiplied with their respective occupation numbers  $f_i$ :

$$\rho(\mathbf{r}) \equiv \rho_s(\mathbf{r}) = \sum_{i=1}^n f_i |\phi_i(\mathbf{r}_i)|^2 \quad (2.25)$$

With eqs. (2.22), (2.24) and (2.25), we have gathered the vital *Kohn-Sham equations*. These effectively allow us to map complex systems of strongly interacting particles onto a single-body non-interacting approximation. Solving many single-body problems thus replaces the computationally demanding job of variationally minimizing the total energy with respect to the density. Recall, that this was already a replacement for the even more daunting task of solving a many-body Schrödinger equation.

In principal, this is a great achievement. In practice, however, one struggles with a cycle of interdependencies: both  $v_H(\mathbf{r})$  and  $v_{xc}(\mathbf{r})$  depend on the density  $\rho(\mathbf{r})$  which itself depends on the single-particle orbitals  $\phi_i(\mathbf{r}_i)$ . These in turn depend on  $v_{\text{ext},s}$  [2, p. 1331] which brings us back to the start since it receives contributions from  $v_H(\mathbf{r})$  and  $v_{xc}(\mathbf{r})$ . The usual solution to this problem is to start with an initial guess to the density  $\rho_{\text{ini}}(\mathbf{r})$  and calculate from this the resulting Kohn-Sham potential  $v_{\text{ext},s}(\mathbf{r})$ . One then solves eq. (2.24) and obtains the corresponding single-particle orbitals  $\phi_i(\mathbf{r}_i)$ . Using eq. (2.25) these orbitals yield a new density with which this process starts anew. After each iteration, the old and new densities are compared until

convergence is reached and all calculated values are consistent (within a predefined margin of error) with their respective dependencies. This procedure is called a *self-consistency cycle* and it is key in numerical DFT-calculations. The point at which convergence is attained is ambiguous. In fact, very different criteria, for example convergence in energy, in density or in another observable entirely can be used to abort a self-consistency cycle. Also, various convergence accelerating algorithms such as mixing of old and new Kohn-Sham potentials after each iteration are in common use [2, p. 1331]. Only rarely does it take more than a hundred iterations to achieve a high level of convergence and even more unusual are instances, where a self-consistent solution cannot be found, perhaps because none exists in the first place. Ultimately, the Kohn-Sham equations remain an approximation to any real world system.

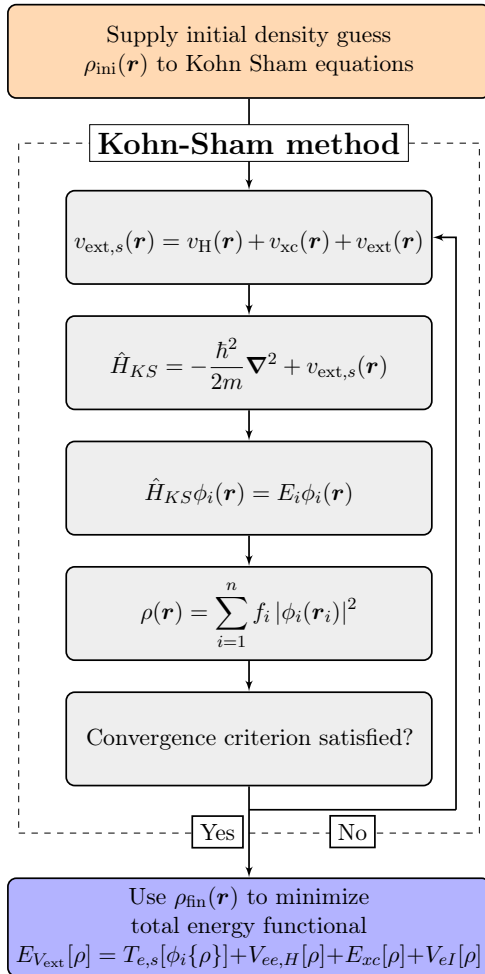


Figure 2.1: Sequence of the self-consistent Kohn-Sham cycle. For most systems, not more than a few dozens cycles are needed to achieve a high degree of convergence.

actual computational DFT. There are a few more helping ingredients, such as pseudopotentials and basis sets yet to cover, albeit from now on more briefly and to the point. First up, pseudopotentials.

Once a sufficiently converged particle density has been obtained in this manner, DFT is back in its element. The total ground state energy can now be derived from eq. (2.15), or more conveniently from<sup>7</sup>

$$E_0 = \sum_{i=1}^n E_i - \frac{1}{2} \frac{e^2}{4\pi\epsilon} \iint \frac{\rho(\mathbf{r})\rho(\mathbf{r}')}{|\mathbf{r} - \mathbf{r}'|} d^3r d^3r' - \int v_{xc}(\mathbf{r})\rho_0(\mathbf{r}) d^3r + E_{xc}[\rho_0] \quad (2.26)$$

It is important to remember in this context that the  $E_i$  are entirely artificial objects lacking physical meaning; they are simply the eigenvalues to those single-particle orbitals  $\phi_i(\mathbf{r})$  that reproduce the many-body density  $\rho_0(\mathbf{r})$ .  $\rho_0(\mathbf{r})$  is the one quantity with strict physical significance in the Kohn-Sham equations [2, p. 1331]. In practice however, this limitation has to be at least partly rescinded: density functional theory is an able tool for calculating band structures. In fact, such calculations were also performed during work on this thesis. For the purposes of convenience, these bands are commonly obtained in DFT by actually calculating the Kohn-Sham eigenvalues  $E_i$ , as they have been found to deliver surprisingly good and useful approximations, even though technically, they are energies of a physically meaningless auxiliary system.<sup>8</sup> This holds especially true for systems that are dominated by local effects with only weak long-range interactions because of the local nature of the employed potential  $v_{ext,s}(\mathbf{r})$ . Strictly speaking, DFT applied in this way is no longer a rigorous many-body theory but rather a mean-field theory [2, p. 1332].

This concludes our discussions on the Kohn-Sham equations. We now have most of the tools necessary for

<sup>7</sup>A derivation for eq. (2.26) can be found in ref. [2, p. 1331]

<sup>8</sup>To obtain a system's band structure, energy calculations are performed along a path through reciprocal space consisting of high symmetry lines, i.e. between  $\Gamma$ -,  $M$ -,  $K$ -Points, etc. Along this path in certain intervals, meaning for certain wave vectors  $\mathbf{k}_n$ , the energies  $E_i(\mathbf{k}_n)$  of the single-particle orbitals are calculated. These values can then be plotted to get a good idea of the system's band structure.

## 2.4 Pseudopotentials and the Projector Augmented Wave Method

One can imagine that having such incisive simplifications as the Hohenberg-Kohn theorem and the Kohn-Sham equations at its foundation makes DFT one of the most computationally efficient many-body theories in solid state physics. As such, it is an especially popular choice among scientists studying large systems with thousands of electrons. To make these endeavours computationally feasible, the concept of pseudopotentials was established. Their development was stimulated by the fact that chemical binding in molecules and solids is very much dominated by the outer valence electrons of each atom [21, p. 243]. The inner lying electrons feel a much more strongly binding Coulomb potential due to their proximity to the nucleus which makes these electrons only weakly chemically active.<sup>9</sup>

This led to the idea of replacing the entire cluster consisting of the core and the tightly bound electrons by an effective ionic potential that acts on the valence electrons and still takes Pauli exclusion into account. These pseudopotentials can be generated in an auxiliary atomic calculation for the element of interest and can then be applied to subsequent molecular or solid calculations. In doing so, one assumes the core electrons are effectively frozen because their orbitals cannot change when the effective ionic potential is held fixed [16, p. 14]. Pseudopotentials are classified as norm-conserving, if the pseudo-wave function they produce coincides well with the real one at distances further away from the potential origin, i.e. the core, than a given cutoff radius  $r_c$ . Such a norm-conserving potential is depicted in fig. 2.2. They are in common use nowadays [22, 23] for reasons we will come back to shortly.

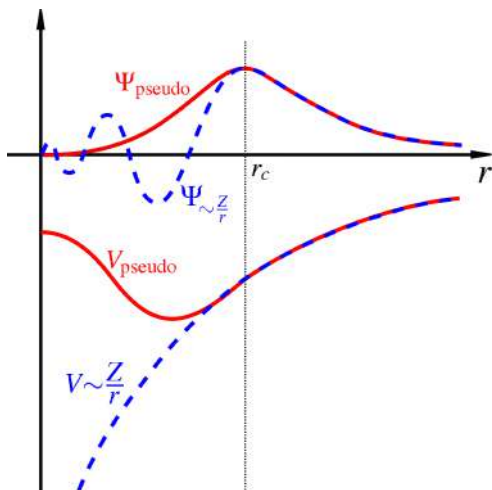


Figure 2.2: Norm-conserving pseudopotential.  $\Psi_{\text{pseudo}}$  and  $\Psi_{\propto \frac{Z}{r}}$  are virtually indistinguishable outside a sphere with radius  $r_c$  around the origin. Taken from [24].

Ideally, the outlying valence electrons are not affected by the introduction of pseudopotentials. Their much lower orbital energies result in comparatively slow phase oscillations  $e^{iEt/\hbar}$  over time, yielding so-called “smooth” wave functions. This property can be exploited, as it makes them ideally suited to be expanded in a plane wave basis set. Plane waves have the distinct advantage of not only being complete in a mathematical sense, but they are also very easy to handle computationally.

Still, it may seem like a rather harsh action to dispense of all near-core physics and replace it with a black box that does nothing except give the appearance of everything being the same at sufficient distance from it. It’s especially problematic when one is interested in information about the core region. Such a scenario is much better addressed by the *augmented plane wave* (APW) method. As the name suggests, it is a progression over simple plane waves. Its essential feature is to divide the space around each nucleus into two disjoint regions [16, p. 14]:

<sup>9</sup>As a result of the small effect of the external potential on core-electron dynamics, the inner lying atomic orbitals strictly present only in isolated atoms are only neglectably perturbed and still deliver a good approximation to core electron wave functions.

- In a certain sized sphere around every nucleus, the electronic orbitals are approximated by atomic wave functions. Space inside such a sphere is referred to as the *muffin-tin region*.<sup>10</sup>
- Any space outside of these muffin-tin regions belongs to the *interstitial region*. Here, the electron form chemical bonds and their orbitals are expanded in the plane wave basis set.

When constructing the interstitial orbitals from plane waves, special care must be put into making the orbitals of both regions connectable, i.e. to achieve a smooth transition of the probability density from one region to another. This is greatly facilitated by norm-conserving pseudopotentials because of the asymptotic relation between pseudo and real wave functions outside the cut-off radius. So the advantages of norm-conserving pseudopotentials mentioned earlier are really twofold: physically, they prevent “jumping” wave functions, which is desirable as these have a tendency of producing unrealistic expectation values, and computationally, the smooth wave functions they produce are much more efficient because computation cost scales with the power of the number of Fourier components, in which the valence functions are expanded [16, p. 14]. Naturally, rough wave functions require more components.

Despite seemingly an intuitive and promising approximation, APW is rarely used. Instead, it is an integral part of a much more wide-spread idea first proposed by Peter Blöchl in 1994, which he dubbed the *projector augmented wave* (PAW) method [25]:

The projector augmented wave method is an extension of augmented wave methods and the pseudopotential approach, which combines their traditions into a unified electronic structure method.

It combines the benefits of both pseudopotentials and APW by keeping the all-electron wave function, meaning no electrons disappear into an effective potential while treating the rapid oscillations of wave functions near the core as localized contributions ranging over the full space. Without getting too deep into it, this is achieved with the help of auxiliary localized functions and projectors [16, p. 14], hence the name.

Of course, other basis sets exist in abundance; a different one optimized for almost every conceivable purpose. The construction of these basis sets is a major enterprise within electronic-structure theory with decades of expertise and a reach far beyond DFT itself. However, they will not be covered in this introduction, since calculations in this work relied solely on the PAW method.

## 2.5 The unknown Exchange-Correlation Functional

As previously discussed in section 2.2, density functional theory is in principal a mathematically exact deduction from fundamental equations of quantum mechanics, mainly the Schrödinger equation. However, this accuracy cannot be maintained in actual DFT calculations. To be practical, these generally require three distinct types of approximations [2, p. 1334]:

1. A conceptual mistake that is made consciously concerns the interpretation of the Kohn-Sham eigenvalues as band energies and their orbitals as actual single-particle wave functions. Strictly speaking, this approximation is optional, as one can simply refrain from interpreting these values at all. However, it is so common that we list it here nonetheless.
2. A numerical error inevitably stems from solving the Kohn-Sham differential eq. (2.24), mainly from the expansion of the single-particle orbitals in the selected basis set (see section 2.4). This error can be reduced to an arbitrary size, if one accepts the corresponding increase in computation time.

---

<sup>10</sup>This name stems from the Muffin-tin approximation, initially proposed by John Slater. In this model, the electronic potential in a solid is assumed to be spherically symmetric inside the muffin-tin regions and constant in the interstitial region.

3. The third type of approximation arises from what is probably the most challenging task in all of density functional theory: constructing a good approximation for the exchange-correlation functional  $E_{xc}[\rho]$ , which contains the entire many-body character of a problem (see eq. (2.15)).

This section will present different solutions to address the third item. More precisely, a brief overview is given of just two different types of approximations to this functional, a local and a semilocal one, that are employed in most DFT-calculations these days. Much more detailed introductions can be found in refs. [18–20, 26–29].

### 2.5.1 Local Density Approximation

Historically, and perhaps also practically, the most important approach to the construction of an exchange-correlation functional is the local density approximation (LDA) [2, p. 1334]. It was conceived in the early days of DFT and published in Kohn and Sham’s famous paper of 1965 [20]. The key idea was to model the exchange-correlation energy for a system containing a homogeneous particle gas satisfying  $\rho(\mathbf{r}) = \rho \in \mathbb{R}$  constant. This brings the advantage that the non-interacting kinetic energy density  $t_s$  in a homogeneous gas is known explicitly. It was derived to be exactly

$$t_s^{\text{hom}}[\rho] = c_t \rho^{\frac{5}{3}}, \quad (2.27)$$

with some constant  $c_t$ . As part of the LDA, this expression is transferred to an inhomogeneous system where  $\rho = \rho(\mathbf{r})$ , so that  $t_s[\rho]$  is approximated locally as

$$t_s[\rho] \approx t_s^{\text{hom}}[\rho] = c_t \rho^{\frac{5}{3}}(\mathbf{r}), \quad (2.28)$$

The total kinetic energy can then be obtained by simply integrating eq. (2.28) over space

$$T_s^{\text{LDA}}[\rho] \equiv \int t_s^{\text{hom}}[\rho] d^3r. \quad (2.29)$$

The kinetic energy approximation  $T_s[\rho] \approx T_s^{\text{LDA}}[\rho]$  is significantly inferior to the exact treatment of  $T_s$  in terms of orbitals, offered by the Kohn-Sham equations [2, p. 1334]. Still, the LDA is very useful as it greatly facilitates the acquirement of another part of the total energy eq. (2.15), namely the exchange-correlation energy,

$$E_{xc}^{\text{LDA}}[\rho] = \int \epsilon_{xc}[\rho] d^3r. \quad (2.30)$$

In eq. (2.30),  $\epsilon_{xc}[\rho]$  signifies the per-volume exchange-correlation energy. This gives an exchange-correlation potential of [16, p. 10]

$$v_{xc}^{\text{LDA}}(\mathbf{r}) = \frac{\delta E_{xc}^{\text{LDA}}[\rho]}{\delta \rho(\mathbf{r})}. \quad (2.31)$$

Here, the facilitation comes into play: for an homogeneous system, the functional of the exchange energy density  $\epsilon_x[\rho]$  can be stated and calculated exactly via [30, p. 8]

$$\epsilon_x[\rho] = -\frac{1}{4} \frac{e^2}{4\pi\epsilon} \int \frac{\rho(\mathbf{r})\rho(\mathbf{r}')}{|\mathbf{r} - \mathbf{r}'|} d^3r. \quad (2.32)$$

Unfortunately, even now, the functional of the correlation energy density  $\epsilon_c^{\text{LDA}}[\rho]$  cannot be explicitly stated. However, numerical values have been calculated for a range of systems, initiated by Quantum Monte Carlo simulations performed by Ceperly and Alder in 1980 [29]. Modern LDA-calculations use fitted analytic expressions of these data points for the correlation energy. A list of these expressions can be found in ref. [18].

As expected, the LDA turned out to be particularly apt for solving systems exhibiting only short ranged effects of exchange and correlation, i.e. solids and other materials whose properties resemble LDA's reference system of an homogeneous particle gas. Yet even for systems that were completely different,  $E_{xc}^{\text{LDA}}[\rho]$  as defined in eq. (2.30) delivered surprisingly good results. It was later discovered that LDA's quality originated at least partly from systematic error cancellation. LDA notoriously underestimates the correlation energy  $E_c^{\text{LDA}}[\rho]$  but overestimates the exchange contribution  $E_x^{\text{LDA}}[\rho]$ , resulting in a realistic value of their sum. At first, this cancellation was assumed to be accidental. Only later was it discovered that for any density  $\rho(\mathbf{r})$ , the LDA-exchange-correlation hole satisfies the correct sum rule, meaning

$$\int \rho_{xc}^{\text{LDA}}(\mathbf{r}, \mathbf{r}') d^3r = -1. \quad (2.33)$$

This trait can only occur, when integrated errors in  $\rho_x^{\text{LDA}}$  clear those of  $\rho_c^{\text{LDA}}$ , which meant that the cancellation was in fact systematic [2, p. 1335].

To sum up the LDA and clarify its part in the conceptual structure of DFT, we should remember that real world systems such as molecules and solids are both inhomogeneous because of the nuclei, and interacting because of Coulomb forces. DFT in the local density approximation tackles this complexity by splitting it up into two simpler problems:

1. a spatially homogeneous but interacting problem (the LDA homogeneous particle gas) and
2. a spatially varying but non-interacting problem (the single-particle approximation described by the Kohn-Sham equations).

From item 1, we obtain the uniform exchange-correlation energy  $\epsilon_{xc}[\rho]$ , which we can then integrate over space, and item 2 delivers the particle density. Both quantities are then connected by the local-density exchange correlation potential in eq. (2.31); via the differential, the exchange correlation energy of the uniform interacting system enters the equations for the inhomogeneous non-interacting system [2, p. 1335].

DFT owes its success partly to this ingenious decomposition of complicated interacting many-body systems. Another part comes from the various possibilities of improving the approximations made by LDA. One such enhancement we will discuss now.

## 2.5.2 Generalized-Gradient Approximation

Another helpful tool in DFT-calculations is the semilocal generalized-gradient approximation [31]. Given an inhomogeneous particle density  $\rho(\mathbf{r})$  (obtained for example in a self-consistent Kohn-Sham cycle) one may, in addition to its value at a given point in space, take into consideration the gradient, i.e. the density's rate of change, in order to calculate local exchange and correlation effects.

Early investigations in this direction showed promise and soon led to a flush of scientific work on the development of new more *general* functionals of both  $\rho(\mathbf{r})$  and  $\nabla\rho(\mathbf{r})$ , which would be able to utilize this extra information. Such functionals of the form

$$E_{xc}^{\text{GGA}}[\rho] = \int f[\rho, \nabla\rho] d^3r, \quad (2.34)$$

have since become known as generalized-gradient functionals. They vary in the choice of  $f[\rho, \nabla\rho]$ , which leads to different GGA-implementations being much more distinct<sup>11</sup> and their results wider spread than say differently fitted LDA-parametrizations [33, 34]. The most popular and also most reliable GGA-implementation in deployment today is one developed by Perdew, Burke and Ernzerhof (PBE) and published in an October 1996 paper humorously named "Generalized

<sup>11</sup>The appendix of ref. [32] contains a collection of explicit expressions for several GGA-implementations.

Gradient Approximation made simple" [31]. In February eight months earlier, Perdew and Burke had shown that a very useful concretization of the energy functional is

$$E_{xc}^{\text{GGA}}[\rho] = \int \epsilon_x[\rho] F_{xc}[\rho, \nabla \rho] d^3r, \quad (2.35)$$

where  $\epsilon_x[\rho]$  again is the correlation energy functional of a uniform gas (as in eq. (2.32)) and the dimensionless quantity  $F_{xc}$  is assumed to be separable into a solely exchange-related and another solely correlation-related part

$$F_{xc}[\rho, \nabla \rho] = F_x[\rho, \nabla \rho] + F_c[\rho, \nabla \rho]. \quad (2.36)$$

Like LDA, the approximation again processes these parts individually by series expansion. The derivation can be found in DFT-literature such as refs. [18, 35]. For brevity's sake, we will not concern ourselves in this introduction.

Over the years, GGA-functionals have been shown to give particularly good results for various types of chemical bonding such as covalent, ionic, metallic and hydrogen bridge [2, p. 1336]. Regrettably, both LDA and GGA fail to correctly reproduce properties of van der Waals bound systems, especially when the long-range asymptotic regime of molecular dipole-dipole interactions comes into play. To address systems with van der Waals governed properties in DFT, a range of specialized approaches were developed and tested (see refs. [11, 36–42]). Because of the importance of van der Waals interactions to the stability of the two-dimensional crystal stackings investigated in this thesis, we will deal with one very simple attempt of extending GGA to make it more van der Waals friendly in the next section.

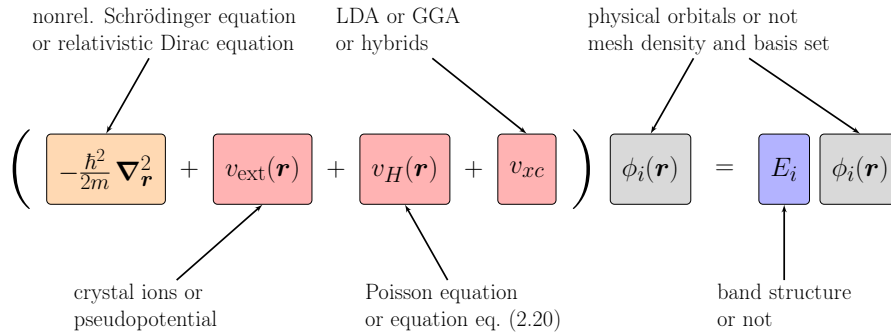


Figure 2.3: Visualization of the wealth of choices one has to make in a DFT-Kohn-Sham calculation. The problem can be handled nonrelativistically based on the classical Schrödinger equation or fully relativistic with the Dirac equation, which includes spin-orbit coupling. The core-near electrons can be modelled explicitly in an all-electron calculation or incorporated along with the nucleus into an effective pseudopotential. The Hartree energy can be obtained by integrating over the charge density or by solving Poisson's differential equation  $\nabla^2 v_H(\mathbf{r}) = -q \frac{\rho}{\epsilon}$  for a system of charge  $q$  (not discussed in the body text, see ref. [7, p. 8]). The exchange-correlation potential can be treated with a huge library of density functionals, LDA and GGA chiefly among them. The exact values of the  $E_i$  can be ignored or be considered approximations to the band structure. Likewise the  $\phi_i(\mathbf{r})$  can be treated as mere auxiliary functions or interpreted as crude approximations to quasi-particle orbitals. The  $\phi_i(\mathbf{r})$  can be computed on a numerical mesh and expanded in one of many possible basis sets, e.g. plane waves, APW, or PAW. Inspired by [2, p. 1334].

## 2.6 Grimme's van der Waals corrections

In solid-state physics, the underlying mechanisms that lead to the formation of bound systems change as a function of a structure's size [41, p. 2]. While chemical bonding is the determining

factor in small molecular systems, its importance decreases as the size increases. Particularly for crystalline assemblies, the importance of weak intermolecular forces can even surpass that of chemical bonding. Research has shown that they are held together either by electrostatic and polarization interactions or, in their (near) absence, by London dispersion forces<sup>12</sup> [41, p. 2]. Since crystalline materials with strong van der Waals interactions make up a considerable share of systems studied with density functional theory, it would be worthwhile to have a method that is suitable for their description. As mentioned before, common density functionals were unable to correctly reproduce effects from dynamical correlations between fluctuating charge distributions [43]. Appreciable progress was made in finding a fully ab-initio treatment of dispersion forces, yet at this point it still remains too computationally expensive to become a routinely used tool on larger systems [41, p. 2]. So in the spirit of DFT, rather than wait for a new theory or better computers to arrive, attempts were made to modify existing density functionals with GGA leading the way.

Perhaps the most promising candidate that emerged out of this regime is the so-called DFT+D-approach (plus dispersion), which stands for a mix of conventional DFT-functionals and an add-on energy term. In essence it simply adds a semiempirical dispersion potential to the conventional Kohn-Sham total energy as defined in eq. (2.15):

$$E_{DFT+D} = E_{KS} + E_{\text{disp}}. \quad (2.37)$$

The dispersion energy correction term  $E_{\text{disp}}$  is a simple function. It takes into account the type of atoms present and their relative interatomic distances. For a periodic (crystalline)  $N$ -atom system, it reads

$$E_{\text{disp}} = -s_6 \sum_{i,j}^N \sum_{\mathbf{L}} \frac{C_6^{ij}}{|\mathbf{r}_{i,0} - \mathbf{r}_{j,\mathbf{L}}|^6} f(|\mathbf{r}_{i,0} - \mathbf{r}_{j,\mathbf{L}}|), \quad (2.38)$$

where  $\mathbf{L} = (l_1, l_2, l_3)$  sums over all translations of the unit cell (where always  $i \neq j$  for  $\mathbf{L} = \mathbf{0}$ ),  $s_6$  is a global scaling-factor,  $C_6^{ij}$  denotes the dispersion coefficient for atom pair  $ij$ ,  $\mathbf{r}_{i,0}$  is the position vector of atom  $i$  in the unit cell at  $\mathbf{0}$  and  $\mathbf{r}_{j,\mathbf{L}}$  that of atom  $j$  in the unit cell reached by a translation of  $\mathbf{L}$ .  $f(|\mathbf{r}_{i,0} - \mathbf{r}_{j,\mathbf{L}}|)$  is a damping function defined as

$$f(|\mathbf{r}_{i,0} - \mathbf{r}_{j,\mathbf{L}}|) = \frac{1}{1 + e^{-d \frac{|\mathbf{r}_{i,0} - \mathbf{r}_{j,\mathbf{L}}|}{R_{ij}^{-1}}}} \quad (2.39)$$

which goes from 0 to 1 as the relative distance  $|\mathbf{r}_{i,0} - \mathbf{r}_{j,\mathbf{L}}|$  between atom pairs is increased. It serves the purpose of scaling the force field such as to minimize contributions from interactions within typical bonding distances [41, p. 4], as these are of course already considered by conventional DFT.

Effectively, the dispersion correction simply adds an additional attractive potential to the result of the DFT electronic structure calculation for each atom pair separated by a distance

<sup>12</sup>London dispersion forces, named after Fritz London, are one of the three types of van der Waals interactions arising between atoms and molecules. Van der Waals forces can be either attractive or repulsive and are classified into three different phenomena:

- the Keesom force between two permanent dipoles.
- the Debye force between a permanent dipole and a corresponding induced dipole.
- London dispersion force between two instantaneously induced dipoles.

Dispersion forces are the strongest of these three contributions in most atoms and molecules. The interaction stems from the outer electrons of adjacent molecules, which try to flee as they repel each other. This causes an oscillating redistribution of electron density in a molecule, i.e. an instantaneously induced dipole. The effect is stronger for larger atoms with bigger shells and also increases with the amount of surface contact, for example between sheets of two-dimensional crystals. The force is called dispersive due to its dependency on the frequency with which the electrons fluctuate.

$$r_{ij} = |\mathbf{r}_{i,0} - \mathbf{r}_{j,L}| \text{ [44, p. 1]}$$

$$E_{\text{disp},ij} = -\frac{C_{ij}^{ij}}{r_{ij}^6} f(r_{ij}) \quad (2.40)$$

In eq. (2.39), the  $R_{ij}$  are called van der Waals radii. These together with the fall-off scale  $d$ , the global scaling-factor  $s_6$ , and the dispersion coefficients  $C_{ij}$ , form the set of fittable parameters that make DFT+D a semiempirical correction scheme.<sup>13</sup> These quantities are adjusted in order to produce real world results in conjunction with a given functional. Various different parametrizations have been constructed in this way to conform with varying exchange-correlation functionals. A version developed by Stefan Grimme et al. in 2004, optimized for use with PBE-functionals, has so far proven especially reliable [45]. In 2006, Grimme published an updated parametrization called DFT+D2 [11] and in 2007 yet another one, DFT+D3 [46], which even takes interactions between triplets of atoms into account to correctly model three-body effects.

Dispersion corrections are only added to the Kohn-Sham total energy after the self-consistency cycle has run its course. Thus, it does not directly affect the wave functions or any other atomic or molecular property. However, forces acting on the atoms in a given configuration are calculated from the gradient of the spatial energy landscape. Inclusion of the dispersion correction alters this landscape and therefore affects the forces acting between atoms. This means that geometry relaxations including lattice constant, cell volume and shape optimizations will differ with and without dispersion corrections.

This concludes our discussions of all of the basic aspects of density functional theory that enable or in some way impact the work of this thesis. The next chapter gives an overview of the DFT package VASP we used to perform all our calculations.

---

<sup>13</sup>For this work, parameter values were used as suggested for DFT+D2 in ref. [11]. In all calculations, the scaling factor was set to  $s_6 = \frac{3}{4}$  and the fall-off to  $d = 20$ .  $C_{ij}^{ij}$  and  $R_{ij}$  obviously depended on the system at hand.

# 3 | The Vienna Ab-Initio Simulation Package

The Vienna Ab-Initio Simulation Package, in short VASP, is a powerful tool, designed specifically for a wide range of density functional calculations. It models atomic scale materials enabling electronic structure calculations and quantum-mechanical molecular dynamics from first principles. It is the instrument of choice for this work because it combines a number of valuable features, among them

- utilization of the projector augmented wave method,
- a plane wave basis set with adjustable completeness, i.e. a freely selectable energy cut-off  $E_{\text{cut}}$ ,
- the use of plane waves enables efficient Fast Fourier Transformation (FFT) for evaluation of  $\hat{H}\phi_i$  terms in reciprocal space,
- construction of computationally efficient periodic systems,
- implementation of the self-consistent Kohn-Sham cycle with both LDA and GGA functionals and
- full geometry relaxations via calculations of the Hellman-Feynman forces.

Besides electronic optimizations using the Kohn-Sham method, the molecular dynamics and relaxation calculation features of VASP were also used in this work. They are implemented within three algorithms following the damped Car-Parrinello method, namely the Quasi-Newton algorithm, the Conjugate Gradient algorithm, and the damped Molecular Dynamics algorithm. They all deal with the problem of minimizing the total energy for a specific geometry iteratively [16, p. 18]. It starts with an initial guess for the ionic configuration for which a Kohn-Sham electronic optimization cycle is performed until a break condition  $\Delta E < E_{\text{break}}$  for the total energy is achieved. After the energy is optimized, the resulting Hellman-Feynman forces are calculated and the ions shifted accordingly, starting a new ionic step until all atoms are relaxed within in a break condition  $\mathbf{F}_J < \mathbf{F}_{\text{break}}$ ,  $J = \{1, \dots, N\}$ , for all  $N$  atoms. In our calculations, the Conjugate Gradient algorithm was used, since it performed particularly well by achieving fast convergence near total energy minima.

The VASP website also states some of the program's important benefits, many of which were covered in chapter 2 [47]

In VASP, central quantities, like the single-particle orbitals, the electronic charge density, and the local potential are expressed in plane wave basis sets. The interactions between the electrons and ions are described using norm-conserving pseudopotentials, or the projector-augmented-wave method. To determine the electronic ground state, VASP makes use of efficient iterative matrix diagonalization techniques [...]. These are coupled to highly efficient Broyden and Pulay density mixing schemes to speed up the self-consistency cycle.

## 3.1 Operation

VASP can be compiled on Unix-compatible systems containing a Fortran90-capable compiler, such as Linux and Mac OS X. It is executed and controlled from a command-line interface. Operation follows a standard procedure. First, a folder is generated containing four key files:

- the INCAR file
- the POSCAR file
- the KPOINTS file
- the POTCAR file

Combined, these files pass on all the necessary information to specify exactly what type of system and calculation shall be carried out by the next VASP run.

The INCAR file in particular is VASP’s central input file. It specifies a large number of parameters and generally determines “what to do and how to do it”. Most of these parameters have convenient defaults, which greatly diminishes the amount of instructions the user has to write. A note of caution: this file is the main source of errors and false results [48].

The KPOINTS file supplies the coordinates and weights of points or the mesh size of a grid in reciprocal space, i.e. the file determines at which wave vectors  $\mathbf{k}_i$  in the Brillouin zone the previously mentioned  $\hat{H}\phi_i(\mathbf{k}_i)$  are evaluated. This can be done by either entering all points explicitly, as Cartesian coordinates (making VASP calculate the corresponding points in reciprocal space itself) or by entering “Line-mode” in which VASP will calculate strings of points (i.e. a path) between supplied points in k-space. This is usually done to obtain band structure information in the form of single-particle energies along lines of high symmetry. Additionally, VASP is also capable of generating grids in k-space automatically which only requires an input for the number of subdivisions along each axis in the Brillouin zone and the origin or shift for the k-mesh [49]. E.g. one would enter

$$\begin{array}{r}
 \text{k-points} \\
 0 \\
 \text{Gamma} \\
 12 \quad 12 \quad 1
 \end{array}
 \tag{3.1}$$

to select an automatically generated (0)  $\Gamma$ -centered (Gamma) grid with 12 samplings along the  $k_x$ - and  $k_y$ -axes and one sampling on the  $k_z$ -axis<sup>1</sup>. This mode was used for most of the calculations in this work.

The POSCAR file determines the entire geometry of the system. It contains all lattice constants and vectors  $\mathbf{a}_i$  and the atomic positions within a unit-cell. The latter can be given either in Cartesian coordinates or as direct coordinates (meaning as coefficients to the lattice vectors),

$$\mathbf{r}_{\text{atom}} = (x_1, x_2, x_3) \quad \text{OR} \quad \mathbf{r}_{\text{atom}} = c_1\mathbf{a}_1 + c_2\mathbf{a}_2 + c_3\mathbf{a}_3
 \tag{3.2}$$

Optionally, it can also provide starting velocities and predictor-corrector coordinates for a molecular dynamics run [50].

Lastly, the POTCAR-file is the only non-user-written input file as these are very large files containing all the information about an atomic species’ pseudopotential. Along with VASP, these files are supplied for every element sorted into several libraries, each library designed to work with a specific functional (i.e. LDA, GGA, etc.). If a system contains more than one atomic species, all necessary POTCAR-files are supplied in the calculation. The POTCAR file also contains information about atomic properties such as mass, valence, energy of the reference configuration for which the pseudopotential was created, etc. They also control the calculation by providing default energy cut-offs  $E_{\text{cut}}$  of the plane wave basis set for all elements [51]. The default values can be overwritten by specifying ENCUT in the INCAR-file.

In the next chapter, a quick introduction to graphene and hexagonal boron nitride is given before we finally proceed to discussing actual results in chapter 5.

---

<sup>1</sup>A single sampling is usually chosen for long (out-of-plane) vacuum directions in real space (without much physics going on) that correspond to short directions in reciprocal space.

## 4 | Graphene and hexagonal Boron Nitride

This chapter serves to give the reader a basic understanding of the materials examined in this thesis while occasionally referring to relevant recent science on graphene and hexagonal boron nitride.

Graphene is an effectively two-dimensional layer of carbon atoms arranged in a hexagonal lattice structure with every carbon atom having three nearest-neighbours at a distance of 1.42 Å [52, p. 1]. It is currently considered the most auspicious candidate for a new generation of nanoelectronics with much higher clock speeds than what is achievable today. With so much at stake, it is small wonder that solid-state physics has plunged into this topic with huge enthusiasm. Science has so far led to fascinating insights into many aspects of graphene, foremost among them its geometric, electronic, mechanic and doping properties.

However, the second constituent of the van der Waals heterostructures that we will examine in this work, the boron nitride, is much less in popular discourse than graphene and not nearly as well researched either. A few interesting facts, however, are already known:

1. Bulk hBN has a layered structure similar to that of graphite [41, p. 11].
2. Within a crystal layer, each boron atom is covalently bound with three nitrogen atoms and vice versa.
3. The BN layers, held together by weak van der Waals interactions, are stacked in such a way that boron atoms are located directly above or below the nitrogen atoms [41, p. 11]. This forms the energetically most favorable electronic state due to the high electronegativity of nitrogen.
4. Unlike semiconducting, high electron transport mobility graphene, h-BN is an insulator with a band gap of  $E_{\text{gap}} = 5.97 \text{ eV}$  [53]. This is caused by the difference in electronegativity between the chemically inequivalent boron and nitrogen sublattices, inducing ionicity and electrons transfer from boron to nitrogen [54, p. 229]
5. It has a lattice constant of  $a_{\text{hBN}} = 2.503 \text{ Å}$  [55] which makes it differ less than two percent ( $\approx 1.8 \%$ ) from graphene's lattice constant<sup>1</sup>.

In our case, particularly items 4 and 5 have farreaching consequences. The highly similar lattice constants make graphene and hBN layers well suited for stacking them on top of each other, creating chemically highly heterogeneous van der Waals bound sandwich-like structures, or short van der Waals heterostructures. The ability to produce such stackings of two-dimensional crystals in a controlled manner would open up a multitude of possibilities for new materials and enable unprecedented command over their exact mechanical and electronic properties.

The question remains what exactly stacking graphene and hBN is expected to achieve and why, in this context, it is significant that hBN consists of highly inequivalent sublattices? To answer this, a short introduction to the history of graphene is in order. Only ten years ago in 2004, it was discovered that a graphene layer can be transferred onto a silicon oxide surface by micromechanical cleavage of high quality graphite [3]. The resulting graphene flakes are micrometers in size, sufficiently large to attach contacts and thus to construct field effect transistors [9, p. 1]. In May 2008, electrical transport measurements performed on single layer suspended graphene at room temperature demonstrated that electron mobilities in excess of  $\mu_{e,\text{gra}} > 200\,000 \frac{\text{cm}}{\text{V}\cdot\text{s}}$  could be achieved [5, p. 3]. This compares to less than  $\mu_{e,\text{si}} < 1400 \frac{\text{cm}}{\text{V}\cdot\text{s}}$  in conventional silicon wafers. Graphene would also likely be able to perform at mobilities in the order of those measured in

---

<sup>1</sup>Graphene's lattice constant is nearly identical to that of graphite, i.e. bulk graphene, whose in-plane lattice constant has been measured in crystallographic x-ray diffraction experiments to be  $a_{\text{gra}} = 2.462 \text{ Å}$  [56]

an experimental setup even when put into a transistor environment with field-induced excess of electrons or holes as these have been shown to scarcely impact electron mobility [3].

Unfortunately, graphene has some downsides, too. Perhaps the single-biggest problem for the implementation of graphene nanoelectronics, especially transistors, are its poor pinch-off characteristics. It is extremely difficult to externally induce two sufficiently distinct states of conductivity. For transistor applications this ability is crucial.

The problem arises due to graphene having a honeycomb structure with two crystallographically equivalent carbon atoms in its primitive unit cell. This makes two bands with  $p_z$  character cross precisely at the Fermi energy at the  $K$  and  $K'$  points in momentum space. As a result, undoped graphene is a zero-gap semiconductor with a linear dispersion relation at the Fermi energy [9, p. 1], called the Dirac point. This anomaly leads to quasiparticles with zero mass, correspondingly called Dirac fermions. Their relativistic nature produces some counterintuitive phenomena. Notably, the term Klein paradox is used to describe the peculiarity that relativistic electrons exhibit perfect transmission through arbitrarily high and wide potential barriers. It is this effect which leads to the altogether incomplete pinch-off of graphene-based FETs [57].

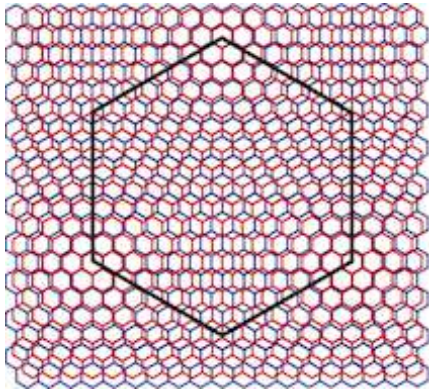


Figure 4.1: A hexagonal moiré structure consisting of many graphene and hBN unit cells with spatially varying superpositions of the two crystals [58, p. 452]. The lattice mismatch is exaggerated by about 10%.

Gianluca Giovannetti et al. explained it best in their 2007 paper [9]:

If one applies a gate voltage so that either holes or electrons are injected into the graphene sheet, the FET is open and its conductivity high. One can then try to block the current by tuning the gate voltage to move the graphene layer toward the charge neutrality point where the Fermi energy coincides with the Dirac points; at this energy, the density of states vanishes and nominally there are no carriers present. However, it turns out that in spite of the lack of electronic states the conductivity does not vanish in this case. Rather, it assumes a minimal value of  $\sigma_{\min} = \frac{4e^2}{h} [\dots]$ . Thus even when pinched off to its maximum the FET still supports an appreciable electrical current, which is intrinsic to graphene and related to the fact that the Dirac fermions are massless.

To close the loop on the difficulties posed by graphene, we summarize that the absence of a band gap prevents the Dirac fermions from attaining a finite mass. This complicates the use of graphene in electronic devices and is directly related to the equivalence of the two carbon sublattices of graphene [59]. Thus, the idea was conceived that in order to suspend this equivalence, one could fuse graphene with another acquainted member of the family of two-dimensional materials, whose sublattices are completely different and who happens to exhibit a similar crystal structure to graphene: hexagonal boron nitride.

In 2007, several theoretical groups commenced ab-initio density functional calculations investigating such heterostructures. Work on this topic is still ongoing today but several things could already be established. Graphene and hBN form a bound system with adhesion energies between  $62 \text{ meV} < E_{\text{adh}} < 83 \text{ meV}$  per unit cell [1, p. 2]. By analyzing the decay of correlation energy functionals for large interlayer spacings, it was also shown that interlayer bonding is indeed

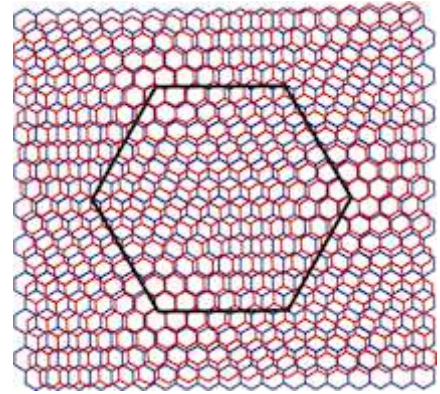


Figure 4.2: Moiré pattern for the same stacking of crystals as in fig. 4.1 but with a small angle of rotation ( $\phi = 3^\circ$ ) between them [58, p. 452]. The lattice mismatch is exaggerated by about 10 %.

due to long-range van der Waals forces [1, p. 2] and that hBN is actually able to directly break the sublattice symmetry, thereby generating an intrinsic and robust mass for the Dirac fermions and even introducing a band gap at the Dirac point in the range of  $7 \text{ meV} < E_{\text{gap}} < 57 \text{ meV}$ , which is roughly twice as large as the thermal energy  $E_{\text{th}} = k_B T \approx 25.85 \text{ meV}$  at room temperature [1, 9]. These two effects give rise to an effective mass for the Dirac fermions of  $m_{\text{Df}} \approx 4.7 \times 10^{-3} m_e$  [9, p. 4].

The opening of a band gap in graphene on h-BN offers the potential to improve the characteristics of graphene-based FETs, decreasing the minimum conductance by orders of magnitude [9, p. 4]. Thus, it seems graphene on hBN might be a real improvement as a transistor material over pure graphene.

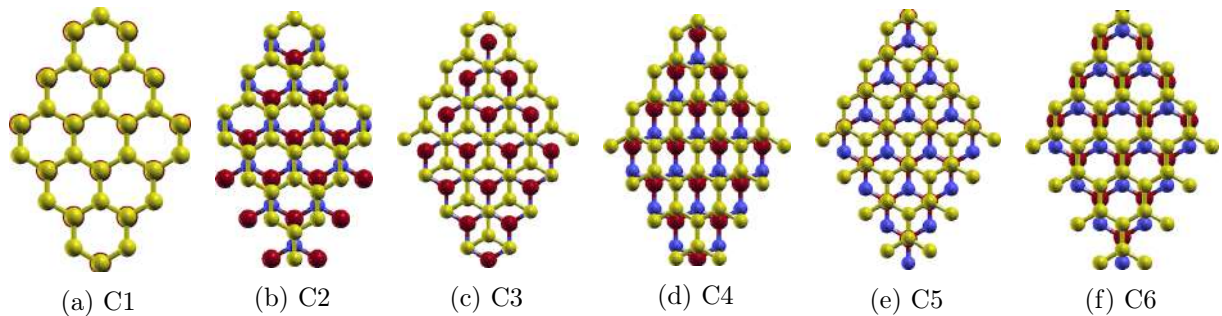


Figure 4.3: Six different stacking configurations of graphene and boron nitride, each chosen to represent the atomic configuration in a certain part of the moiré cell depicted in fig. 4.4.

Up to this point, we have ignored the possibility that the lattice mismatch of graphene and hBN might introduce unexpected behaviour. In fact early calculations commonly used either graphene's or hBN's lattice constant or a value in between for both crystal. Only later was it found out, that this is energetically not the most favorable state, as it would require the carbon atoms in graphene to all slightly stretch apart while the boron and nitrogen atoms in hBN would have to close ranks. Because both single layer graphene and hBN are remarkably stiff with reported two-dimensional Young's moduli of  $Y_G = 340 \frac{\text{N}}{\text{m}}$  and  $Y_{\text{hBN}} = 309 \frac{\text{N}}{\text{m}}$  [1, p. 3] respectively, the energy gain from increased interlayer van der Waals attraction is not sufficient to pay for the high in-plane deformation energy cost of both materials. As a result, it should be expected that the lattice mismatch persists when applying graphene onto hBN and strain be released by realizing spatially varying stacking configurations, giving rise to so-called moiré structures (see figs. 4.1 and 4.2). This realization served to explain why scanning tunneling microscopy experiments at the time were seeing large regularly arranged hexagonal shapes [60, 61].

The reader should also note that due to the upheld lattice mismatch and the resulting spatially varying crystal configurations, every calculation in this thesis was carried out for six different stackings, each representing a certain area within the moiré cell in fig. 4.1. The six configurations are shown in fig. 4.3. From one stacking to the next, the graphene lattice is shifted downward by

half a B-N bond length. The goal is to obtain a good impression of the in-plane variation of all calculated quantities.

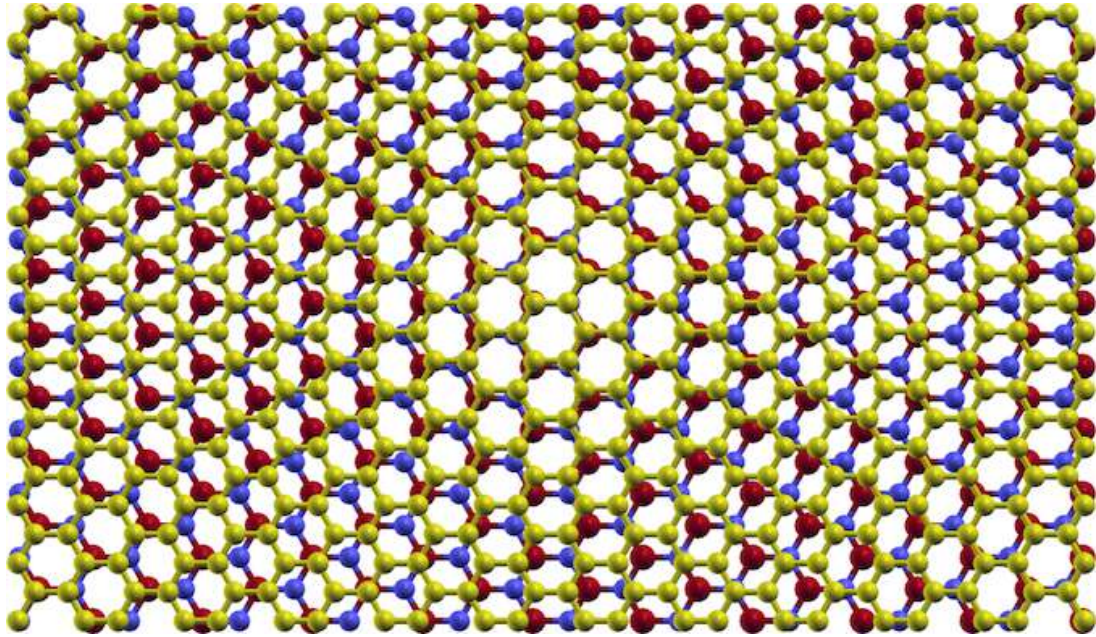


Figure 4.4: Moiré pattern of graphene-hBN

As a side note, when graphene and hBN are fused in real-world conditions, the two lattices are typically not aligned in such a way as depicted in fig. 4.1. Their crystallographic axes can be rotated relative to one another by an arbitrary angle, as shown in fig. 4.2. This possibility has only been explored experimentally very recently (April 2014) but produced rather interesting results. Apparently, the size of the moiré cells shrinks with the angle of rotation. Woods et al. performed atomic force microscopy, reporting that  $\phi \approx 0^\circ$  corresponded to a moiré periodicity of  $L \approx 14$  nm whereas  $\phi \approx 1.5^\circ$  produced a moiré structure with  $L \approx 8$  nm [58, p. 452]. In the former case ( $\phi \approx 0^\circ$ ), they measured the typical moiré pattern exhibiting all six configurations known from previous studies [60, 61]. However, for  $\phi \approx 1.5^\circ$ , measurements were entirely different. The lowest energy layout achievable was no longer the incommensurate state in which each layer retains his own lattice constant. Instead, it was found that large moiré-cell sized hexagonal areas surrender the lattice mismatch, thereby becoming commensurate and completely assume configuration C5. As a result, these areas accumulate strain along their diameter, which is released in thin walls with completely different crystal configurations separating the C5 regions. This is shown fig. 4.5. [58, p. 452]. Woods et al. described the physics behind this commensurate-incommensurate transition as a function of  $\phi$  as follows:

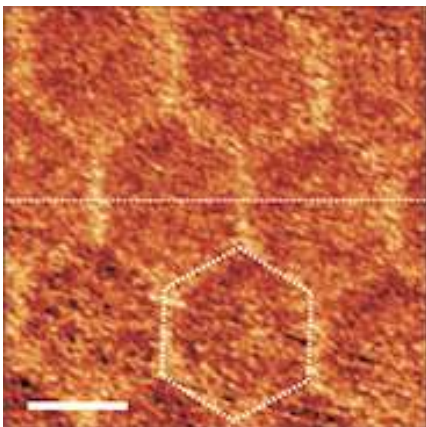


Figure 4.5: Young's modulus distribution measured with an atomic force microscope in PeakForce mode displaying 14 nm sized moiré cells separated by thin white walls with considerably higher Young's modulus, meaning less elasticity [58, p. 453]. The white scale bar is 10 nm in length.

If the relative rotation angle between the two crystals is small (large period of the moiré pattern), it becomes energetically favorable to adjust the two lattices to become commensurate, losing in elastic energy but gaining in van der Waals energy. The latter decreases if preferred atomic positions are achieved over the whole area. When  $\phi$  increases past some critical value (so that the period of the moiré pattern becomes small), the gain in van der Waals energy can no longer compensate for the elastic energy and the two crystals act independently, forming an incommensurate state.

At this point, we are finally done with establishing groundwork. In the next chapter, we will start looking at the results obtained during work on this thesis.

# 5 Results and Discussion

With the theoretical knowledge of chapter 2 and the short introduction to VASP in chapter 3 at our back, we will now take a look at some of the results obtained during this project. We start with total energy curves as a function of the distance between the crystal sheets that comprise our heterostructure, graphene and hBN. From this, we derive certain properties under strain, particularly the Young’s modulus. Lastly, we supply information on the band structure with a particular focus on the band gap and dispersion relation at the Dirac cone. For everyone of these characteristics, we compare the performance of regular LDA and GGA in combination with Grimme’s DFT+D2 implementation.

## 5.1 Relaxation of Graphene on hexagonal Boron Nitride

Initially, we performed a full relaxation calculation to obtain a structural geometry optimized for our particular choice of functional, basis set, pseudopotential, and  $k$ -mesh. To simulate the graphene-hBN system in VASP, we used periodic boundary conditions and constructed a unit cell consisting of two carbon atoms on top of one boron and nitrogen atom each with roughly 20 Å of vacuum above. Six stacking configurations were considered (see fig. 4.3): starting from C1, the graphene sheet was translated downward by half a C-C bond length in each step until the initial configuration was reached again [1, p. 2]. These configurations were specifically chosen to represent certain equally distributed areas within the incommensurate moiré structures that graphene-hBN heterostructures have been observed to form [1, 60, 61]. We will compare these six areas of the moiré throughout our discussion to obtain an overview of the spatial variation of graphene-hBN’s properties.

The lattice constant was chosen as  $a_{\text{G,LDA}} = 2.465 \text{ \AA}$ , referring to the LDA-optimized lattice constant of graphene. This is slightly smaller than the LDA-optimized lattice constant for hBN  $a_{\text{hBN,LDA}} = 2.490 \text{ \AA}$  [1, p. 2] but arguably close to the common lattice constant for graphene on free-standing hBN  $a_{\text{G-hBN}} = 2.467 \text{ \AA}$  [1, p. 3]. During the relaxation, the two carbon atoms fixated while all three boron and nitrogen coordinates were allowed to relax. VASP was instructed to perform a local density approximation based on the Ceperley-Alder exchange-correlation functional using a gamma-centered  $k$ -point mesh of  $12 \times 12 \times 1$  points. We further chose a plane-wave basis set with an energy cut-off at  $E_{\text{cut}} = 400 \text{ eV}$  and a global break condition for the electronic self-consistent-loop of  $E_{\text{diff}} = 10^{-4} \text{ eV}$ .<sup>1</sup>

Configuration	C1	C2	C3	C4	C5	C6
$d_{0,\text{LDA}} [\text{\AA}]$	3.58	3.39	3.36	3.30	3.21	3.27
$d_{0,\text{RPA}} [\text{\AA}]$	3.54	3.50	3.50	3.43	3.31	3.45

Table 5.1: Equilibrium interlayer distances for graphene-hBN in all six configurations as calculated by the LDA and RPA. RPA-data was kindly provided by ref. [63].

As the lattice constant was already optimized, in-plane atomic positions relaxed only negligibly. However, we found equilibrium interlayer distances changed appreciably from our initial guess of 3.1 Å and also showed a strong dependence on the configuration. Results are shown in table 5.1 and compared with corresponding data obtained in the random-phase approximation (RPA) using the framework of adiabatic connection fluctuation-dissipation theory (ACFDT) [1]. We find good

<sup>1</sup>VASP aborts relaxation of the electronic degrees of freedom if the total energy change and the band structure energy change between two steps are both smaller than  $E_{\text{diff}}$  [62].

agreement between both methods with RPA predicting on average 3% larger separation. Both agree on C1 having the largest and C5 the smallest interlayer separation. This quality of results from a local density approximation surprises. By comparison, ACFDT-RPA is a computationally very demanding process. Unlike LDA and GGA it makes no local or semilocal approximations and is therefore much better suited for the modelling of systems with long-range van der Waals interactions. Consequently, one can expect it to deliver highly accurate results, particularly for van der Waals heterostructures [64, 65]. This assumption is supported by good agreement between theory and experiment where it was possible to compare them so far [1, 58]<sup>2</sup>.

## 5.2 Total Energy Calculations

In order to determine each configuration's energy as a function of the interlayer distance  $d$  between the two crystal layers, self consistent LDA and GGA calculations were performed. To model electron-electron exchange and correlation, the local density approximation continued to rely on the Ceperley-Alder functional whereas the generalized gradient approximation employed a popular parametrization by Perdew, Burke and Ernzerhof. Total energies were calculated for the following interlayer separations:

- in steps of 0.025 Å from 2.5 to 5 Å,
- in steps of 0.25 Å from 5.1 to 7.5 Å,
- in steps of 1.25 Å from 8 to 12.5 Å,

The  $k$ -point mesh was refined from  $12 \times 12 \times 1$  to  $24 \times 24 \times 1$  points. Additionally, VASP options  $E_{\text{diff}} = 10^{-6}$  eV and NELMIN = 4 were provided to lower the total energy break condition (previously  $E_{\text{diff}} = 10^{-4}$  eV) and to force VASP to perform at least 4 loops in the self-consistency cycle even if the break condition is already achieved. This prevents VASP from unwantedly falling into a local secondary minimum of the total energy and taking it to be the global one. Such an occurrence would terminate a calculation prematurely, producing imprecise results and hence rough energy curves. All other settings remained (see section 5.1).

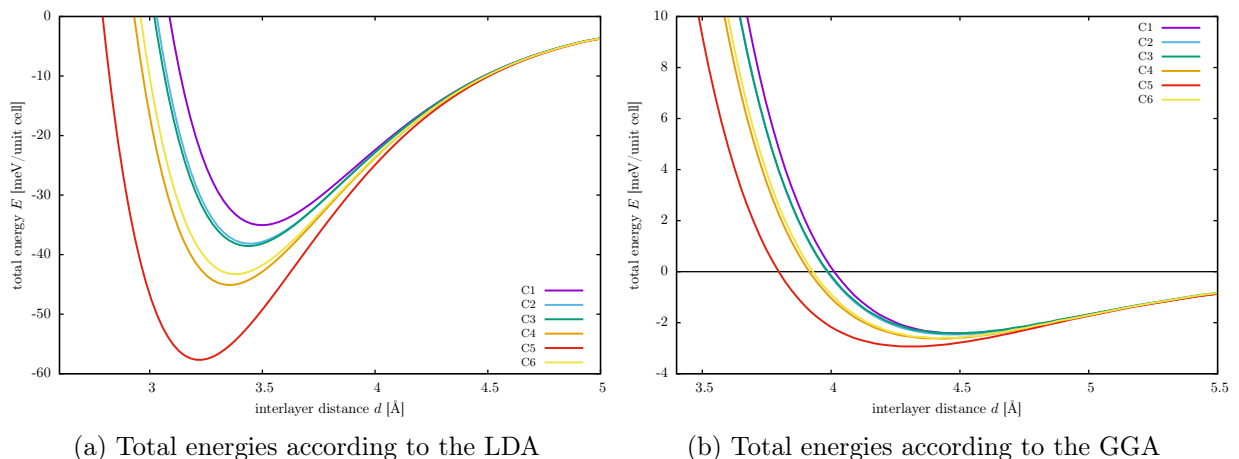


Figure 5.1: Comparison of the total ground state energy per unit cell as a function of the interlayer spacing  $d$  for six different stackings. All curves are shown relative to a zero point energy defined by the total energy of both layers at large separation.<sup>3</sup>

<sup>2</sup>In ref. [7], the RPA was used to calculate local variations of the Young's modulus across the moiré periodicity of graphene on hBN. They found data in the range of 26.0 to 31.5 GPa [7, p. 71]. Very recently, ref. [58] substantiated these claims with experimental data. They were only able to measure relative variations but found the amplitude to be roughly 10% of the total Young's modulus [58, p. 453].

### 5.2.1 LDA

Figures 5.1a and 5.1b show the LDA and GGA total energies per unit cell relative to the energy at large separation as a function of the interlayer spacing  $d$  for the different crystallographic configurations. There is a noticeably different curvature in both figures. LDA predicts a much stronger interlayer binding caused by substantial total energy minima whereas GGA curves are much shallower, resulting in an only marginally bound compound of graphene and hBN.

Within the LDA, C1 is the highest-energy configuration, exhibiting a minimum of 35 meV at an interlayer separation of 3.50 Å, whereas C5 is by far most favorable energy-wise and very closely bound, with a minimum of 58 meV at 3.23 Å. Going from C1, C5 is approached stepwise both in energy and separation in the order C2, C3, C6, and C4. This concurs with the configurational order found by [1, p. 2]. Interestingly, C2 and C3 are virtually indistinguishable for all interlayer spacings. C4 and C6 also show strong conformity. However, both findings are likely to be accidental, as there are no apparent structural similarities. C5's unit cell has one carbon atom sitting directly on top of a boron atom while the other one rests above the center of a boron-nitrogen hexagon (leaving nitrogen completely uncovered). A possible explanation for the high stability could be that this allows on average more electrons to adopt an energetically favorable state close to the strongly electronegative nitrogen. In any case, this finding suggests that commensurate states as reported by ref. [58] for graphene-hBN heterostructures with small rotation angles should appear predominantly in C5 as it has the highest ability to compensate strain energy costs stemming from the thin walls of built-up tension that separate commensurate hexagons (see fig. 4.5). We further propose that C4 and C6 are closest to C5 in energy because these configurations also do not cover nitrogen but rather form a carbon ring around it, making it approachable for many electrons.

Looking now towards large layer separation in fig. 5.1a, we find, as expected, that above 4.5 Å, all configurations become energetically indistinguishable. This allows the interesting conclusion that varying layer displacements have no measurable effect on van der Waals interactions over these distances. Mind, this should not be confused with the statement that van der Waals interactions do not appreciably affect the system across these distances. In fact, ref. [1, p. 2] was even able to refute such a claim, demonstrating that the RPA correlation energy  $E_c^{\text{RPA}}$  does not follow an exponential falloff for large layer separations  $d$ , as would be expected from local correlation effects included in LDA or GGA. Instead, calculations showed  $E_c^{\text{RPA}} \propto d^{-4}$  which coincides with theoretical predictions of the correlation energy decay for van der Waals bound two-dimensional insulating systems [66, 67]. For completeness, all LDA minimum total energies and their corresponding equilibrium layer distances are presented in table 5.2.

Configuration	C1	C2	C3	C4	C5	C6
$d_{0,\text{LDA}}$ [Å]	3.50	3.45	3.43	3.35	3.23	3.38
$E_{0,\text{LDA}}$ [meV]	35.05	38.16	38.55	45.10	57.68	43.29

Table 5.2: Equilibrium layer distances and binding energies per unit cell as calculated in the LDA for different stackings

### 5.2.2 GGA

By contrast, GGA produces extremely weak binding between 2.4 meV per unit cell at an interlayer distance of 4.51 Å for C1 and 2.9 meV at 4.29 Å separation for C5. Such a system is unable to cohere under room-temperature conditions ( $k_B T \approx 25$  meV). As such, these values can only be dismissed as unrealistic, considering the fact that experiments have found graphene and

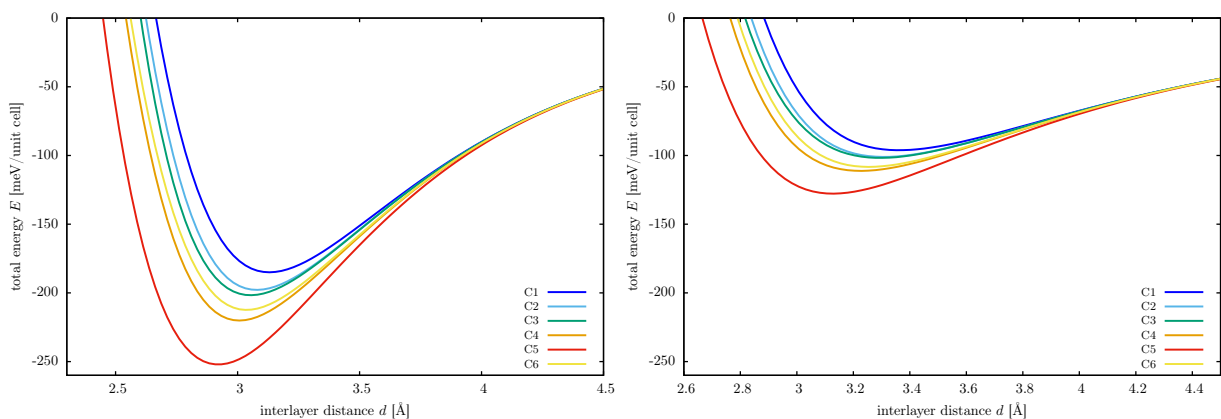
<sup>3</sup>Throughout this thesis, the zero point energy was calculated from the ground state energy  $E_0$  at  $d = 12.5$  Å.

hBN to form stable compounds. Moreover, it does not compare favorably to RPA calculations performed by ref. [1, p. 2], which yielded binding energies per unit cell of graphene on hBN in the range of 62 to 83 meV and equilibrium layer distances of 3.31 to 3.54 Å, depending on the configuration. This indicates that GGA separations in the range of 4.3 to 4.5 Å are significantly overestimated. Interestingly, not only the absolute but even the relative differences in energy between configurations is much smaller for GGA than for LDA or RPA: the former predicts  $E_{0,C5}$  to be about 21 % larger than  $E_{0,C1}$ , whereas it is around 65 % and 34 % for LDA and RPA respectively. Apparently, the GGA models graphene-hBN as a system with very little interaction between crystal sheets and the interaction that does occur scarcely depends on layer displacement.

These results should again be surprising, though this time not due to their high but rather low quality, especially considering the fact that GGA is actually an advancement over LDA and often produces more reliable results [31, 68]. The most likely cause for this is an error cancellation that occurs in the LDA exchange-correlation functional, which is suspended by using the more general GGA functionals. A remark that possibly explains this behavior was given on page 18 in chapter 2. It is worth noting however, that despite the lack of even qualitative agreement between LDA and GGA, the configurational order does not change. From high to low energy, it is still C1, C2, C3, C6, C4, C5. Besides, C2, C3 and C6, C4 are still very similar, with the former two even covering each other in fig. 5.1b. C5 again exhibits the strongest binding by a significant margin. All GGA values for the equilibrium layer distances and corresponding binding energies are shown in table 5.3.

Configuration	C1	C2	C3	C4	C5	C6
$d_{0,GGA}$ [Å]	4.51	4.46	4.49	4.44	4.29	4.41
$E_{0,GGA}$ [meV]	2.42	2.46	2.43	2.62	2.93	2.61

Table 5.3: Equilibrium layer distances and binding energies per unit cell as calculated in the GGA for different stackings



(a) Total energies according to the LDA with Grimme's corrections

(b) Total energies according to the GGA with Grimme's corrections

Figure 5.2: Comparison of the total ground state energy per unit cell as a function of the interlayer spacing  $d$  for six different stackings.

### 5.2.3 LDA with Grimme's corrections

In light of such poor results, it seems especially worthwhile to investigate whether (semi-)local approximations can be improved efficiently using Grimme's semiempirical van der Waals

corrections in such a way as to correctly model heterostructures, and graphene on hBN in particular. Grimme’s DFT+D2 method [11, 45] was designed to remedy DFT’s inherent inability to correctly describe van der Waals interactions resulting from dynamical correlations between fluctuating charge distributions [69]. Fortunately, all fittable parameters in Grimme’s approach have been tuned specifically so as to work in combination with the GGA functionals designed by Perdew, Burke, and Ernzerhof [31], which we used for all GGA calculations. These parameters were not intended to be used in combination with LDA. However, this is no obstacle that would prevent the enthusiastic theorist from testing their performance with LDA anyway. Solely with the intent of conducting a systematic investigation, we did so as well.<sup>4</sup> DFT+D2 is implemented into VASP and can be engaged by simply adding the flag `LVDW = .TRUE.` to the INCAR file. As a first test of Grimme’s corrections on graphene-hBN, we simply repeated the self-consistent calculations from sections 5.2.1 and 5.2.2.

The results are shown in figs. 5.2a and 5.2b. LDA in combination with Grimme’s DFT+D2 approach, henceforth LDA+D2, now produces binding energies roughly 4 to 5 times bigger than before (compare tables 5.2 and 5.4) and more than twice as large as GGA+D2. Binding energies for different parts of the moiré range from 185 to 212 meV per unit cell, where the most strongly bound areas again adopt C5 and the weakest binding appears in C1. The configurational order in between remains the same, though it appears curves are a little more equally distributed. For example, in the LDA C5 displayed an about 28 % lower energy than the next most strongly bound configuration C4. In LDA+D2, this relative difference shrinks to just 14 %. Moreover, the equilibrium interlayer distances are considerably shifted to the left. Whereas values were in the range of 3.2 to 3.5 Å without Grimme’s correction, the two layers are now predicted to converge much closer with distances around 2.9 to 3.1 Å. For comparison, we again resort to the previously mentioned findings obtained in RPA-calculations by ref. [1] which predicted binding energies of 62 to 83 meV and 3.31 to 3.54 Å for the equilibrium layer distance. We conclude that LDA+D2 produces overbinding and yields considerably undersized layer separations.<sup>5</sup> All binding energies and equilibrium interlayer distances obtained with LDA+D2 can be found in table 5.4.

Configuration	C1	C2	C3	C4	C5	C6
$d_{0,\text{LDA+D2}}$ [Å]	3.13	3.08	3.08	3.01	2.91	3.03
$E_{0,\text{LDA+D2}}$ [meV]	185.03	197.84	201.34	220.12	252.02	212.38

Table 5.4: Equilibrium layer distances and binding energies per unit cell as calculated in the LDA+D2 for different stackings

#### 5.2.4 GGA with Grimme’s corrections

From the GGA+D2 energy curves in fig. 5.2b we gather strong interlayer interaction for all configurations due to binding energies between 96 meV per unit cell for C1 and 128 meV per unit cell for C5. This is much weaker binding than what was predicted by LDA+D2. However it still denotes an overbinding when compared to RPA, which found, averaged over all configurations, binding energies roughly 55 % lower. However, this still counts as a noticeable improvement over standalone GGA, which had previously failed almost entirely in predicting a bound state for graphene on hexagonal boron nitride. When it comes to structural information or at least the equilibrium interlayer distance, GGA+D2 seems to be an even bigger improvement. Values lie in a very realistic domain of 3.15 to 3.35 Å, making them only slightly smaller than the RPA results shown in table 5.1 which ranged from 3.31 to 3.54 Å. We therefore conclude that in the

<sup>4</sup>Future studies could evaluate to which extent a parameter adjustment might improve performance when combining LDA with Grimme’s corrections.

<sup>5</sup>We don’t blame Grimme for this profound overestimation of van der Waals effects as he never had LDA in mind when developing his method.

special case of graphene-hBN, GGA when augmented with Grimme’s corrections performs much better than on its own, even approaching more expensive RPA data. Precise GGA+D2 results for binding energies and equilibrium interlayer distances of all six stacking configurations are given in table 5.5.

Configuration	C1	C2	C3	C4	C5	C6
$d_{0,\text{GGA+D2}}$ [Å]	3.35	3.30	3.30	3.23	3.13	3.25
$E_{0,\text{GGA+D2}}$ [meV]	96.14	101.05	101.73	111.21	127.78	108.31

Table 5.5: Equilibrium layer distances and binding energies per unit cell as calculated in the GGA+D2 for different stackings

We also point to the fact that LDA+D2 and GGA+D2 agree on the energetic order of different stackings. From high to low energy, the order in both cases is C1, C2, C3, C6, C4, C5, which also concurs with RPA and regular LDA. This could be initial support for an interesting hypothesis claiming two things, namely the existence of a *monotonic* function mapping between energy predictions of different methods and secondly, that energies in different methods that form image and pre-image pairs with respect to this function belong to the same configuration. Of course, this could only be true, if no two configurations exhibit exactly the same energy. As a clarifying example, assume we have an energy  $E_{\text{LDA}}$  calculated in the LDA and know an explicit expression for the above mentioned function going from, say LDA to RPA, now called  $f$ , then we could calculate the corresponding energy  $E_{\text{RPA}}$  via

$$f : \{ \langle \Psi | \hat{H}_{\text{LDA}} | \Psi \rangle | \Psi \in \Omega_{\text{LDA}} \} \rightarrow \{ \langle \Psi | \hat{H}_{\text{RPA}} | \Psi \rangle | \Psi \in \Omega_{\text{RPA}} \}, \quad (5.1)$$

$$f[E_{\text{LDA}}(C_i)] = E_{\text{RPA}}(C_i)$$

and we would know that those energies belong to the same configuration. In eq. (5.1),  $\Psi$  stands for a wave function belonging to the systems configurational space  $\Omega$ . To make a more definitive claim, it would require much more data on how energies correspond to crystal configurations for different methods.

Putting those thoughts aside, we summarize that cheap local approximations like regular LDA and van der Waals corrected GGA serve sufficiently well, even when compared to computationally intense nonlocal methods when only qualitative comparison of different system configuration is required. With this conclusion, we end our discussion on total energy curves. All four methods compared in this section will continue to be deployed. In the next section, we will look at what each has to say about the elastic properties of different moiré areas.

### 5.3 Young’s modulus

The Young’s modulus, named after 19th century British scientist Thomas Young, characterizes the stiffness of an elastic material. It is defined as the ratio of the stress along an axis over the resulting strain (in the range of stress in which Hooke’s law holds) so that stiff materials achieve high Young’s moduli. Here, stress is defined as force per unit area and the strain is the ratio of deformation over the initial length. Young’s modulus is the most common elastic quantity, but there are others, such as the bulk modulus and the shear modulus [70]. Specifying the Young’s modulus is only meaningful if its axis is stated as well or if it is clear from the context. Here, we will concern ourselves solely with the interlayer Young’s modulus; so when talking about strain and stress, they are always to be understood as along the axis perpendicular to both the graphene and hBN sheet.

The Young’s modulus is experimentally accessible. It has even been measured very recently for the case of graphene on hBN by using atomic force microscopy to literally pull up and push

down a graphene sheet on an hBN substrate [58]. It can also be extracted from the total energy curves presented in the previous section by calculating the second order derivative with respect to the interlayer distance  $d$  at the equilibrium layer distance  $d_0$ . Introducing the uniaxial interlayer strain  $\epsilon$ , which expressed in terms of the interlayer distance reads

$$\epsilon = \frac{d - d_0}{d_0}, \quad (5.2)$$

we can write the Young's modulus as follows:

$$Y = \frac{1}{d_0} \frac{1}{A_0} \left. \frac{\partial^2 E_{\text{str}}(\epsilon)}{\partial^2 \epsilon} \right|_{\epsilon=0} \quad (5.3)$$

Here,  $A_0 = 5.24 \text{ \AA}^2$  is the equilibrium unit cell area of graphene on hBN,  $E_{\text{str}}$  is the strain energy per unit cell and  $d_0$  was found to be around 3 to 3.5  $\text{\AA}$  (see section 5.2). We obtained the function  $E_{\text{str}}(\epsilon)$  from a polynomial fit. All fits were performed using gnuplot.<sup>6</sup>

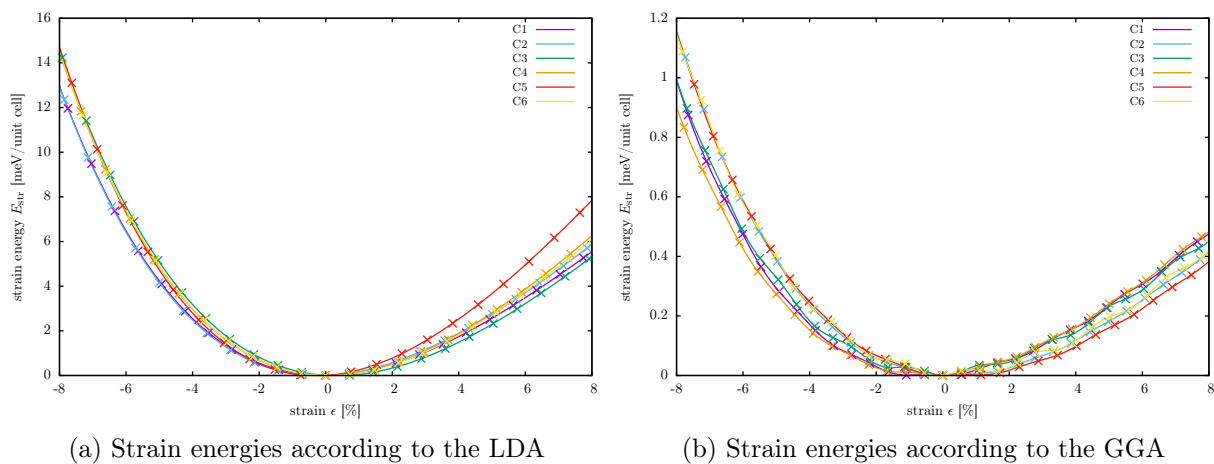


Figure 5.3: Strain energy  $E_{\text{str}}$  per unit cell as a function of strain in different areas of the moiré pattern

### 5.3.1 LDA and GGA

Figures 5.3a and 5.3b show the LDA and GGA strain energies per unit cell for the different stackings. Essentially, these plots show the same data, as the total energy curves in figs. 5.1a and 5.1b but zoomed in on the total energy minimum, with a shifted zero point energy and a linear transformation of the abscissa according to eq. (5.2). The points show the total energies as calculated by VASP for varying interlayer distances of graphene on hBN and the connecting lines are 7th-degree polynomial fits produced with gnuplot. Fitting functions including inharmonic terms were necessary to account for the clearly visible compression-tension-asymmetry exhibited by both LDA and GGA strain energies.

As was to be expected from the radically different binding behaviour predicted by LDA and GGA, their strain energies also vary significantly. While a local density approximation produces between 12 to 14 meV strain energy per unit cell at  $-8\%$  strain (compression), the semilocal approximation amounts to only 0.9 to 1.2 meV strain energy per unit cell. In the case of LDA, this compares favorably to RPA findings of 15 to 18 meV per unit cell at  $-8\%$  strain [7, p. 71].

<sup>6</sup>It processes high order polynomials with an implementation of the nonlinear least-squares (NLLS) Levenberg-Marquardt algorithm (LMA) [71]. Like most numeric minimization algorithms, LMA is an iterative procedure. For reasonable starting parameters, it tends to be slower than other options [72]. However, it is distinguished by a high robustness; it manages to find solutions even if it starts far off the final minimum.

We again attribute most of the difference between LDA and GGA to GGA’s lack of the same error cancellation that takes place in all LDA calculations. In truth, both LDA and GGA suffer the same methodical inability to correctly model van der Waals bound systems. We suppose that the introduction of gradient dependent functionals simply makes this problem more apparent.

Young’s moduli corresponding as per eq. (5.3) to the fit functions in figs. 5.3a and 5.3b are shown in table 5.6. Both LDA and GGA predict C5 to have the highest Young’s modulus (meaning it offers the highest resistance upon tension or compression). However, we find the familiar discrepancy of more than one order of magnitude between their quantitative outcomes. LDA’s prediction of 30.47 GPa is remarkably close to RPA data obtained in ref. [7, p. 71] which stated 31.5 GPa for C5. Both values are slightly lower than in graphite, where the Young’s modulus perpendicular to the graphene sheets was found experimentally to be about 37 GPa [73]. This is likely a good indicator for the quality of these findings since bulk materials commonly exhibit a slightly higher mechanical stiffness than their two-dimensional counterparts. Thus, we interpret GGA’s Young’s modulus of 1.46 GPa for C5 as another deterrent for using standalone GGA on van der Waals heterostructures.

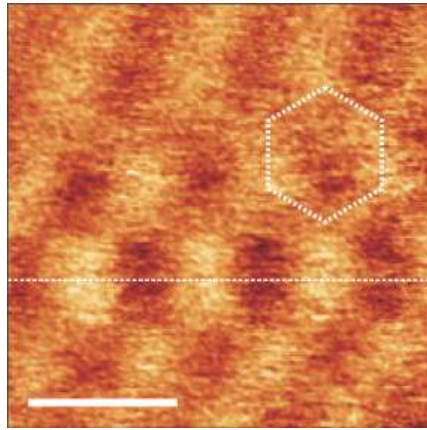
Configuration	C1	C2	C3	C4	C5	C6
$Y_{\text{LDA}}$ [GPa]	22.57	23.26	25.13	26.78	30.47	26.36
$Y_{\text{GGA}}$ [GPa]	1.36	1.44	1.31	1.28	1.46	1.45
$Y_{\text{RPA}}$ [GPa]	26.2	26.6	26.0	27.7	31.6	27.7

Table 5.6: Young’s moduli for the different stacking configurations according to LDA and GGA. Comparison with RPA results from ref. [63].

As observed before from the minimum total energies in tables 5.2 and 5.3, LDA and GGA do not agree on the configurational order from lowest to highest Young’s modulus. For LDA it is C1, C2, C3, C6, C4, and C5 and therefore the same order as found in the binding energy (see table 5.2). For GGA, we find C4, C3, C1, C2, C6, to C5 (see table 5.3), which is entirely different from what we found in our total energy investigations. Considering GGA’s performance so far, one should wield caution, when trying to attest physical significance. More likely, this variation stems from the fact that with GGA binding energies so low, the total energy curves run very shallow. Small errors in VASP’s operations (produced possibly by an insufficiently small break condition) can then introduce unphysical curls into GGA’s total energy curves. In fact, we find visual proof by looking at fig. 5.3b which displays vacillating strain energy curves whereas in fig. 5.3a, LDA curves are even. Going back further, this can already be surmised if one looks closely at C3 and C6 in fig. 5.1b. Presumably, these curls are then picked up by the fitting function (7th-degree polynomials provide highly flexible fits), leading to localized fluctuations of the fitting function’s derivatives and thus to fluctuations in GGA’s Young’s moduli.

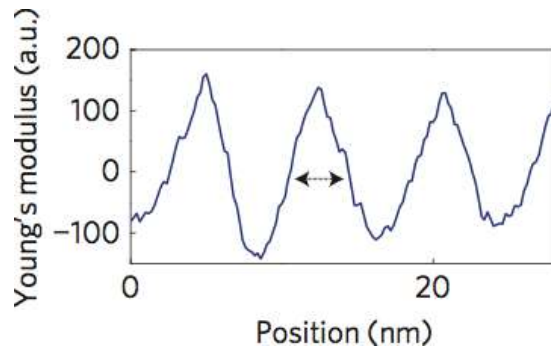
Another interesting observation can be made from the data in table 5.6. For both methods, the Young’s modulus displays a high spatial variation of more than 10% within different areas of the moiré. As a result, the rigidity of graphene sheets against decohesion from hBN should vary within the moiré [7, p. 70], displaying a sinusoidal modulation over space with a period equal to that of the moiré itself. This theoretic prediction is in qualitative agreement with observations from contact-mode AFM experiments conducted by ref. [58, p. 453]. Figure 5.4 shows measurements performed on an 8 nm moiré with the periodic variations of the Young’s modulus displayed in fig. 5.4b.

As an incidental remark, the modulated adhesion energy landscape should lead to the generation of minor in-plane displacements of graphene atoms. This supports our findings in



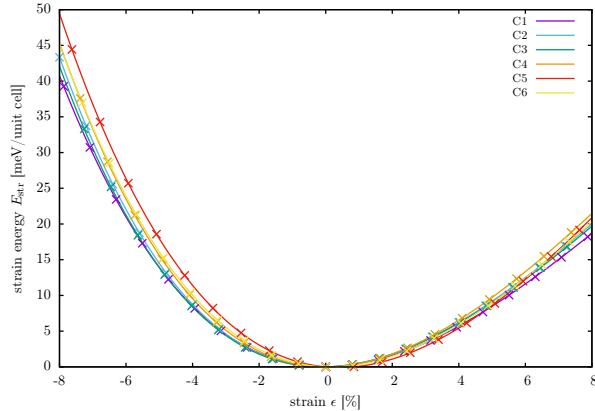
(a) Young's modulus distribution, measured in the PeakForce mode, for an 8 nm moiré. The white scale bar is 10 nm in length.

Figure 5.4: Experimental AFM observations of moiré patterns and Young's modulus oscillations for graphene on hBN. Figures 5.4a and 5.4b are taken from ref. [58, p. 453]

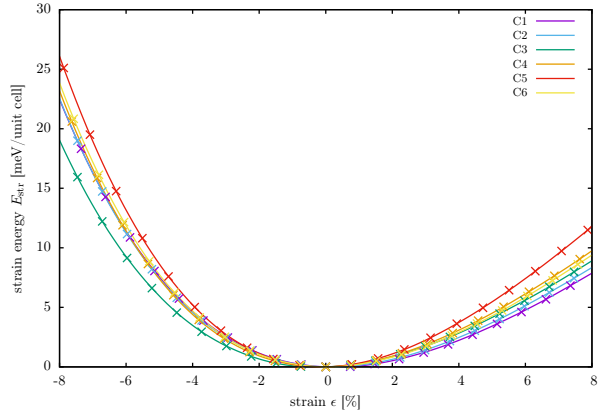


(b) Cross-section of the Young's modulus distribution taken along the dashed line in fig. 5.4a.

section 5.2, where all four deployed methods predicted different equilibrium layer distances for different crystallographic configurations. Corrugation of graphene on hBN lay in the range of about 0.2 to 0.3 Å (due to interlayer spacings of 3.23 to 3.50 Å for LDA and 3.13 to 3.35 Å for GGA+D2). The corrugation is distributed across the moiré, with a periodicity of about 14 nm for sheets without relative rotation [58, p. 452]. Thus, resulting planar deformations in graphene are much less than 0.01 pm per graphene primitive unit cell [7, p. 72]. Although this effect turns out to be very small, it is currently investigated whether plane corrugations could be important for the incommensurate-commensurate transition observed by ref. [58] [7, p. 71].



(a) Strain energies according to the LDA



(b) Strain energies according to the GGA

Figure 5.5: Strain energy  $E_{\text{str}}$  per unit cell with Grimme's corrections as a function of strain in different areas of the moiré pattern

### 5.3.2 LDA and GGA with Grimme's corrections

Strain energies for LDA and GGA calculations incorporating Grimme's van der Waals corrections are shown in figs. 5.5a and 5.5b. At  $-8\%$  strain, the energy cost is now much bigger with 40 to 50 meV for LDA+D2 and 18 to 26 meV for GGA+D2. This was to be expected because strain energy costs scale with a systems stability and sections 5.2.3 and 5.2.4 showed van der Waals corrected systems to be more strongly bound than their uncorrected counterparts. Unfortunately, such high strain energies as predicted by LDA+D2 fail to coincide with RPA studies, where values from 15 to 18 meV per unit cell at  $-8\%$  strain were found for the different configurations

Configuration	C1	C2	C3	C4	C5	C6
$Y_{\text{LDA+D2}}$ [GPa]	84.28	89.97	87.00	99.81	107.71	98.61
$Y_{\text{GGA+D2}}$ [GPa]	37.54	38.68	35.15	42.19	52.78	42.35
$Y_{\text{RPA}}$ [GPa]	26.2	26.6	26.0	27.7	31.6	27.7

Table 5.7: Young’s moduli for the different stacking configurations according to LDA and GGA incorporating van der Waals interactions. Comparison with RPA results from ref. [63].

[7, p. 71]. GGA+D2 results on the other hand are closer to RPA. Averaged over all configurations, it delivers strain energies roughly 33% larger than RPA.

The curve fits in figs. 5.5a and 5.5b were used to calculate Young’s moduli with corresponding values listed in table 5.7. LDA+D2’s strong overbinding produced interplanar Young’s moduli between 84 to 108 GPa. For a two-dimensional sheet of material this is unrealistic and another sign that Grimme’s corrections are not sufficiently robust to perform well at modelling van der Waals heterostructures in conjunction with LDA. The intended partner for Grimme’s corrections, namely GGA with PBE functionals performed better, predicting Youngs moduli of 35 to 53 GPa. However, except for C3, all configurations have a higher Young’s modulus than the 37 GPa experimental value obtained for graphite [73], which indicates that the overbinding produced by GGA+D2 affects its predictions towards elastic properties. As such, GGA+D2 can only deliver a crude impression of what to expect from a new material in experiment.

So much for strain energies and Young’s moduli. In the next section, we will continue to compare the performance of LDA and GGA when used on graphene-hBN, this time in the context of band structures.

## 5.4 Band Structure and Band Gap

Due to its sublattice symmetry, graphene is a semiconductor with vanishing intrinsic band gap. In contrast, hexagonal boron nitride consists of fundamentally different boron and nitrogen sublattices, making it an insulator with a band gap of 6 eV [53]. In ref. [1, p. 2], the decay of the correlation energy was shown to follow a power law of  $E_c^{\text{RPA}} \propto d^{-4}$  signaling that van der Waals forces are the dominant contribution in producing a bound system rather than purely local interactions which should result in an exponential fall-off for the correlation energy. Despite the relative weakness of van der Waals forces when compared to other interactions, the electronic states of graphene can be considerably modified by the presence of an hBN sheet [7, p. 60]. This is due to the mutual van der Waals interactions producing effectively a spatially inhomogeneous external potential acting dissimilarly on electrons of different atoms. This breaks graphene’s sublattice symmetry, thereby inducing an intrinsic band gap at the Dirac point and giving the quasi-particle Dirac fermions an effective mass of around  $4.7 \times 10^{-3} m_e$  [9, p. 4]. This effect offers graphene-hBN the potential to achieve a more complete room temperature pinch-off than pure graphene-based field effect transistors. With improvement in fabrication techniques and an enhanced understanding of the subtleties of doping effects, this could eventually allow for a minimum conductance reduction by orders of magnitude [9, p. 4].

For this reason, band structure and band gap investigations in particular have always constituted an integral part of graphene research. Since system behavior in this regard is so strongly van der Waals dependent, it should be particularly interesting to take a closer look in the present section at how dispersion corrected LDA and GGA perform in this area; not only from a methodical stand point but also physically. To keep things short, we will concern ourselves with configuration C5 at the equilibrium layer distance only.

## 5.4.1 LDA and GGA

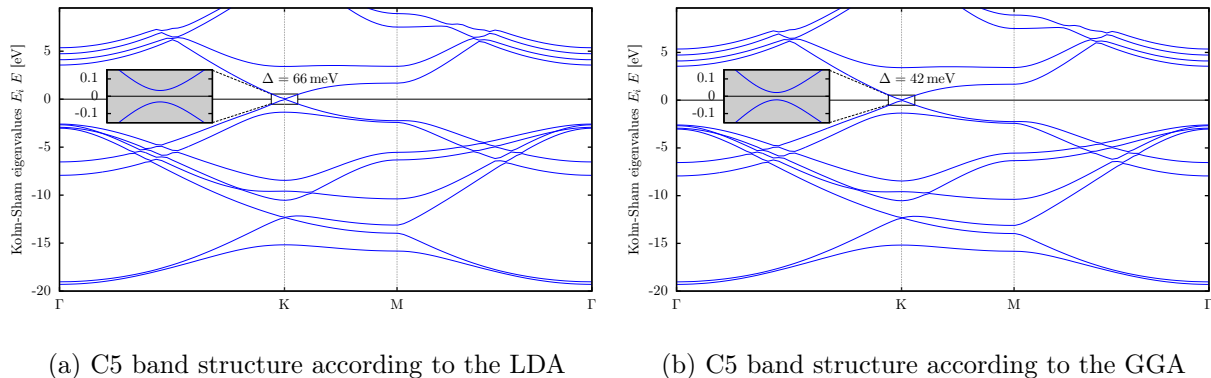


Figure 5.6: Band structure along a path of high symmetry through the graphene-hBN Brillouin zone of configuration C5 in a relaxed state

For our band structure calculations, we changed VASP’s  $k$ -space sampling behavior by switching from a  $k$ -point grid into line-mode. We calculated bands along a closed path of high symmetry lines in reciprocal space, sampled at 150 regular intervals equaling steps of roughly  $0.02/\text{\AA}$ . This proved sufficient to deliver smooth band structure data. In the INCAR file, we set `ICHARG = 11`, which suppresses the self-consistency cycle and instructs VASP to read the charge density from a previous calculation. All other VASP settings were left untouched.

In figs. 5.6a and 5.6b, we see C5 band structures of graphene-hBN as obtained from regular LDA and GGA calculations. Bands are shown for a relaxed system at the equilibrium interlayer spacing. The plots appear very similar, indicating that there is little difference in the single-particle Kohn-Sham eigenvalues between LDA and GGA. Near the Fermi level, figs. 5.6a and 5.6b display graphene  $p_z$  low-energy states with a very similar appearance to the dispersion of suspended graphene. Due to hBN’s considerable band gap, its states only occur at energies well below ( $< -1$  eV) and above ( $> 3$  eV) the Fermi level. The  $p_z$  states protruding (in real space) from the crystal planes appear to be unaltered at this resolution. Only at a closer look (see gray insets) do the modifications become visible. Sublattice symmetry breaking has indeed produced a band gap, albeit small, directly at the Dirac point. It measures 66 meV and 42 meV for LDA and GGA respectively. We also find directly below the valence band maximum and below the conduction band minimum, the graphene specific linear dispersion is suspended and replaced by a parabolic behavior [7, p. 62]. This concurs with experimental findings of a small band gap and parabolic dispersion around the Dirac point of graphene on an hBN substrate gathered by ref. [9, p. 3].

Band structures were also calculated for the five remaining configurations and evaluated with regard to their band gap. Resulting data for equilibrium interlayer distances is shown in table 5.8. We find here that the more strongly bound system modelled by LDA produces larger band gaps. This was expected since a more strongly bound system implies more interaction between its components. Therefore, the van der Waals potential acting differently on identical carbon sublattices is also stronger, causing a more complete symmetry breaking and thus a larger band gap. GGA, which exhibited almost no binding in our total energy calculations (see figs. 5.1a and 5.1b), leads to smaller, but still considerable band gaps slightly above 40 meV. The fact that GGA’s band gaps are substantial is surprising. A possible explanation is that even an extremely weakly bound system still features non-neglectable symmetry breaking.

For comparison, table 5.8 also contains band gap data obtained by LDA energy calculations on RPA optimized structures (simply labelled RPA for the purposes of differentiation) as taken from [7, p. 63]. Looking at the big picture, we see that  $\Delta_{\text{LDA}}$  and  $\Delta_{\text{RPA}}$  both exhibit very strong variation depending on the configuration.  $\Delta_{\text{GGA}}$  on the other hand appears only slightly affected

Configuration	C1	C2	C3	C4	C5	C6
$\Delta_{\text{LDA}}$ [meV]	71.23	18.71	60.78	63.94	65.80	91.02 <sup>M</sup>
$\Delta_{\text{GGA}}$ [meV]	42.13	40.55	42.15	42.29	42.14	43.80
$\Delta_{\text{RPA}}$ [meV]	57	7 <sup><math>\Gamma</math></sup>	34	25 <sup>M</sup>	47	14 <sup>M</sup>

Table 5.8: Band gaps for graphene states at the  $K$  point as calculated in the LDA and GGA. A superscript  $M$  ( $\Gamma$ ) indicates that this band gap was detected to be shifted towards the  $M$  ( $\Gamma$ ) point.  $\Delta_{\text{RPA}}$  was obtained by ref. [7, p. 63] from LDA calculations on RPA optimized crystal geometries.

by layer displacement. This results in a very steady band gap across the length of the moiré unlike the sinusoidal variation observed for the Young’s modulus in fig. 5.4b. Considering GGA’s poor performance on graphene-hBN, we don’t expect this to be confirmed by experiment. When comparing our results to RPA data, we find large divergence. LDA generally predicts the largest gap with an average of  $\bar{\Delta}_{\text{LDA}} = 61.91$  meV, more than twice as much as  $\bar{\Delta}_{\text{RPA}} = 30.67$  meV and still roughly 50% larger than  $\bar{\Delta}_{\text{GGA}} = 42.18$  meV.

Going into more detail, there is virtually no agreement between methods. Configuration C2 has the smallest gap for all three, even marking a drop to as low as  $\Delta_{\text{LDA},\text{C2}} = 19$  meV and  $\Delta_{\text{RPA},\text{C2}} = 7$  meV. This is where the similarities end. We find no consensus on which configuration has the largest band gap. While according to LDA and GGA, moiré areas exhibiting C6 have the largest band gap with 71 meV and 44 meV respectively, RPA predicts this to be C6 with a band gap of 57 meV. There is also no qualitative agreement on the order of the configurations. This is even more discordant than what was found so far in comparisons of the total energy and the Young’s modulus.

During our investigations, we occasionally witnessed an interesting phenomenon. In some configurations, the Dirac cones were not located directly at the  $K$ -point in reciprocal space but rather shifted towards the  $M$ -point or in the other direction towards the  $\Gamma$ -point. In table 5.8, these are indicated by a superscript “ $M$ ” and “ $\Gamma$ ” respectively. This phenomenon is likely another effect of the suspended threefold symmetry of the graphene nearest-neighbor bonds due to the presence of hBN. Interestingly, we only found this behavior for Configuration C6. Ref. [1, p. 3] also reported small shifts of the Dirac cone within the hexagonal Brillouin zone, but in three cases instead of one: C4 and C6 were shifted away from the  $K$  to the  $M$  point, and in the opposite direction for C2. This disparity can likely be attributed to our relatively low sampling rate of 50 intervals per high-symmetry line, requiring the offsets to be quite large in order to be detected. At this point, we must assume not all shifts were registered.

#### 5.4.2 LDA and GGA with Grimme’s corrections

We now turn towards band structure calculations incorporating van der Waals corrections. Structures obtained in the LDA+D2 and GGA+D2 for C5 in its equilibrium state are plotted in figs. 5.7a and 5.7b respectively. We again find the results to be highly similar between both methods and unaltered at this large scale when compared to the same method without dispersion corrections. This is due to the post-processing nature of Grimme’s corrections. Energies resulting from the sum over pairwise forces are only added onto the total system energy after the self-consistent cycle has run. Therefore, the Kohn-Sham Eigenvalues are not influenced directly. They change only slightly owing to different equilibrium interlayer distances when incorporating van der Waals interactions. However minute, these differences appear when looking at the Dirac point on a sub-electronvolt level.

Here, LDA+D2 produces a large band gap of 144 meV which is almost twice as large as the 78 meV GGA+D2 equivalent. When we measure this by the standard of LDA band structure calculations on RPA optimized geometries, we find both to be substantially oversized. Such

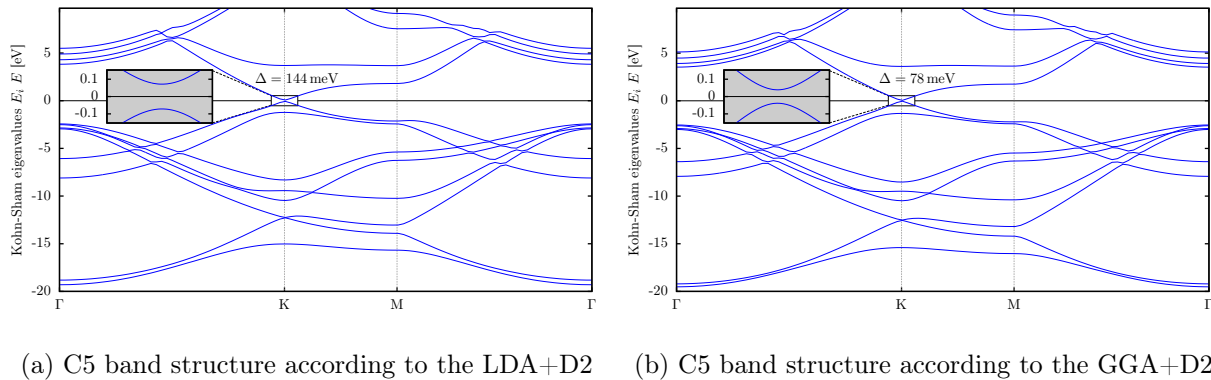


Figure 5.7: Band structure along a path of high symmetry through the graphene-hBN Brillouin zone of configuration C5 in a relaxed state

calculations were carried out by ref. [7, p. 63] and found an equilibrium band gap of 47 meV for C5. Like before, especially LDA+D2 sticks out with its unrealistic claim that is more than 200 % larger, yet again demonstrating that even the enthusiastic theorist should not be using Grimme’s dispersion corrections in combination with LDA. GGA+D2’s band gap is still 66 % larger, indicating that there is still much room for improvement of Grimme’s implementation when used on heterostructures.

We show band gap data for the remaining configurations in table 5.9. Somewhat surprisingly in the light of the findings of previous sections, qualitative agreement between methods has partly improved with the introduction of van der Waals corrections. While before, predictions for the largest band gap were equivocal, now all three methods concur on C1 for this characteristic. This does not extend to a quantitative comparison though. LDA+D2 predicts a massive 213 meV and GGA+D2 still issues 101 meV. That is about 4 and 2 times larger than the reference value of 57 meV. Unfortunately, we still cannot report agreement on the configurational order.

Configuration	C1	C2	C3	C4	C5	C6
$\Delta_{\text{LDA+D2}}$ [meV]	213.39	161.71	148.51	121.07 <sup><math>\Gamma</math></sup>	143.66	156.01 <sup><math>M</math></sup>
$\Delta_{\text{GGA+D2}}$ [meV]	101.35	50.89	77.91	78.52	77.65	92.65 <sup><math>M</math></sup>
$\Delta_{\text{RPA}}$ [meV]	57	7 <sup><math>\Gamma</math></sup>	34	25 <sup><math>M</math></sup>	47	14 <sup><math>M</math></sup>

Table 5.9: Band gaps for graphene states at the  $K$  point as calculated in the LDA+D2 and GGA+D2. A superscript  $M$  ( $\Gamma$ ) indicates that this band gap was detected to be shifted towards the  $M$  ( $\Gamma$ ) point.

All things considered, our comparisons in this section have painted a mostly cautionary picture. Predictions of local approximations on a graphene-hBN system should be considered unreliable, regardless of whether or not Grimme’s semiempirical corrections for dispersion forces are included. In the next and perhaps most interesting part of our evaluation, we will stack up all five methods against each other graph by graph in a single plot and see who fares best in approaching RPA, which we assume to reflect reality.

## 5.5 Method Comparison

Both LDA and GGA are known to underestimate the binding energies of van der Waals dominated structures [1, 41, 74] and mispredict decay towards large interlayer distances [1, p. 3] because they do not correctly account for attractive long-range van der Waals interactions. As the main purpose of this thesis, it was investigated whether semi-empirical van der Waals corrections

(detailed in section 2.6) might constitute a computationally efficient alternative to expensive fully ab-initio nonlocal methods, such as ACFDT-RPA.

Figure 5.8 gives an at-a-glance view of the prospects of this proposition by directly comparing the output of LDA, GGA, LDA+D2, GGA+D2 and RPA. Figure 5.8 focuses on the total energy with varying layer separation for graphene-hBN's lowest energy configuration C5 only. Like before, all curves are shown relative to the energy at large interlayer separation (12 Å of vacuum).

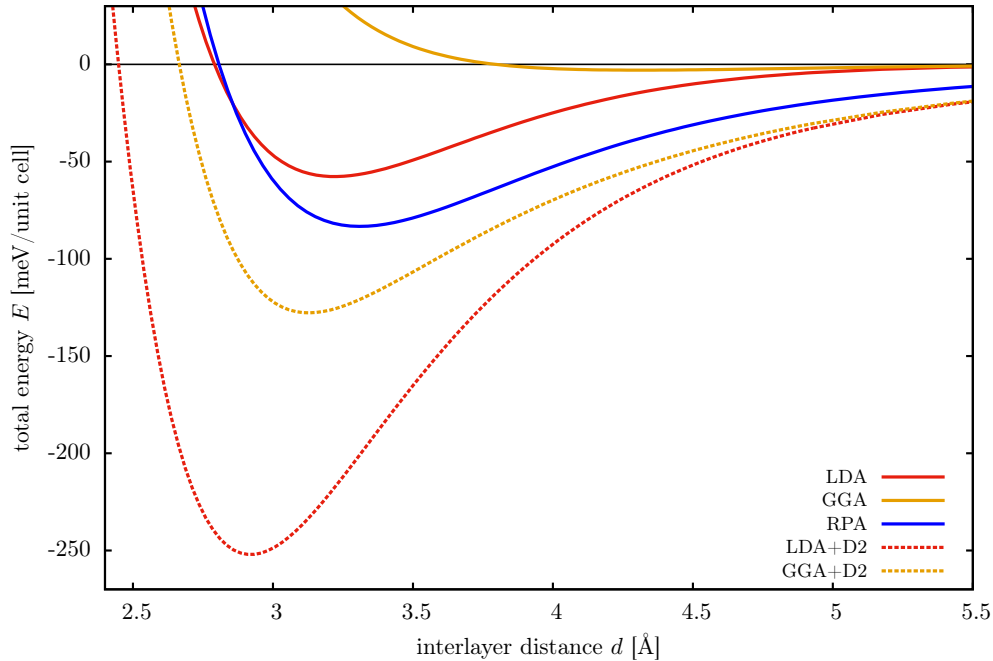


Figure 5.8: Methodical comparison of LDA, GGA and RPA via total energies for C5 as a function of the interlayer distance  $d$ . RPA data was kindly provided by ref. [1].

Unfortunately, we find that none of the graphs align closely with RPA. Therefore, we cannot report achievement of finding such an alternative. It is quite obvious that GGA and LDA+D2 are particularly inapt for use on graphene-hBN. However, depending on the required accuracy, we suggest that regular LDA and GGA+D2 can still be suitable for the investigation of van der Waals heterostructures. We substantiate this assessment based on the following findings:

1. Figure 5.8 shows that RPA, LDA, and GGA+D2 have curves of similar shape. Our discussions in previous sections demonstrated that this often implies qualitative agreement between their predictions of strain energies, Young's moduli and band gaps.
2. GGA+D2 (and even LDA+D2) is clearly an improvement over noncorrected local approximations in reproducing RPA's asymptotic behaviour. For large separations, LDA and GGA display an exponential decay<sup>7</sup> much faster than that of RPA. Accounting for van der Waals interactions via D2, this turns into a power-law decay approaching RPA for large  $d$ .
3. Despite GGA's considerable overestimation of equilibrium interlayer distances (4.29 to 4.51 Å), we found GGA+D2 predictions of 3.15 to 3.35 Å to lie very close to RPA's 3.31 to 3.54 Å (see section 5.2.4). This suggests that D2 performs especially well on structural data.
4. Throughout our investigations, we found particularly standalone GGA to have difficulties correctly reproducing relative differences of the binding energy, Young's modulus and band gap between configurations (see fig. 5.1b and tables 5.6 and 5.8). After adding dispersion corrections, this improved substantially, becoming much closer to RPA predictions (see fig. 5.2b and tables 5.7 and 5.9).

<sup>7</sup>Local and semilocal approximations only account for correlations between overlapping states which decay exponentially in vacuum [75, p. 2, 7, p. 57].

There is also the prospect of improvement of GGA+D2, which we do not count into the above list, as it still requires extra work at this time. Besides their computational efficiency, D2 corrections have the advantage of being semiempirical in nature. While this makes them unfit for reliable predictions on a new type of system (as we learned during our investigations and especially from fig. 5.8), it enables a high degree of versatility and straightforward improvement of this method: performance depends entirely on the choice of parameters. RPA currently stands as by far the best method for van der Waals heterostructures, achieving excellent agreement with experiment in multiple cases such as graphite and bulk hBN [64, 65]. It is therefore ideally suited to serve as a benchmark when optimizing D2. By comparing GGA+D2 to RPA, it is possible to systematically analyze, how strongly GGA+D2 output depends on parameters and even more relevant, to find a better set of parameters for use on heterostructures. Note that Grimme et al. derived their implementation mostly from testing on noncovalently bound complexes such as large stacked aromatic molecules and group II element clusters [11].

Finally, a potentially useful fact that should not be overlooked in fig. 5.8 is that LDA and GGA+D2 energy curves envelope RPA. LDA's binding remains weaker than RPA's for most interlayer spacings, underestimating adhesion by about 30%. This agrees with refs. [66, 76], where LDA binding energies are shown to be systematically too low in graphite, in contrast to the common belief that LDA effects an overbinding [7, p. 57]. On the other hand, GGA+D2 overestimates binding across all separations. Together, they could serve a purpose in defining upper and lower bounds for the total energy and other quantities derived thereof. On small systems well suited for investigation in the RPA, this is not needed. The fact remains though, that LDA and GGA have the advantage in computational efficiency and are therefore capable of treating larger systems. Thus, our findings could be helpful for studies occurring frequently in physical chemistry where the objective is to study van der Waals systems too large for RPA.<sup>8</sup> Interestingly, despite LDA and GGA+D2 producing opposite misbinding, we find both to underestimate the equilibrium interlayer distance by 3.6% and 6.6% (in the case of C5) respectively.

In conclusion, fig. 5.8 demonstrates the importance of using methods like RPA, that by construction incorporate long-range correlations in an ab-initio fashion. Although GGA+D2, originally designed for structural optimizations, proved reliable in finding equilibrium layer separations (see table 5.5), we found standalone LDA to work even better in this context. For system information beyond spatial layout such as elastic properties and band gaps, we found LDA and GGA+D2 predictions to be less dependable. Therefore we state that for cases, where highest possible accuracy and reliability on such quantities is sought, LDA and GGA with or without Grimme's corrections should not be the methods of choice for graphene-hBN, and presumably not for other van der Waals heterostructures either. This can be considered an urge to caution in light of the current perception of dispersion corrections and their reliability. Recent statements in the DFT community claimed for example that "dispersion corrections lead to significant improvements in accuracy and the computational cost associated with them are negligible. [...] there is little reason not to use them." [79].

---

<sup>8</sup>In the past, chemistry relied on multi-step empirical methods often involving a high degree of parametrization for large system studies [77, 78].

## 6 | Summary and Outlook

Van der Waals heterostructures - sandwich-like stackings of two-dimensional crystals essentially resembling molecular lego - are in frequent discourse nowadays and likely to remain one of the leading topics in condensed matter physics and materials science for some time to come [80]. A diverse library of fundamental building blocks is already available with new ones appearing thanks to intense research. Their precisely chosen layer by layer assembly creates the possibility for a nearly unlimited number of designs and variations. The first already remarkably complex heterostructures have recently been fabricated, revealing enhancements and recombinations of the already unusual traits of their compounds, among them extremely high carrier mobility in the case of graphene [81], valley-selective circular dichroism in molybdenum disulphide [82] and potentially the first two-dimensional magnetic crystal in the form of monolayer  $\text{K}_2\text{CuF}_4$  [7, p. 126]. Other characteristics were entirely new and unexpected, leaving the door wide open for exciting new phenomena science may yet discover. However, for this to happen, it requires extensive experimental investigations intelligently guided by preceding theoretical insight. Thus it is vital for theory to have at its disposal appropriate tools for modelling these systems.

This proved to be a challenge when binding of two-dimensional crystal compounds was shown to rely on long-range van der Waals interactions [1, p. 2]. As such, it marks a serious issue for popular and well-established local and semilocal approximations, i.e. LDA and GGA. Other possibilities exist that by construction incorporate long-range exchange and correlation effects and are therefore much better suited to describe van der Waals heterostructures. One such method that has been demonstrated repeatedly to achieve very good agreement with experimental data [1, 41, 58, 83, 84] and was used for comparison purposes throughout this thesis is the adiabatic connection fluctuation-dissipation theory (ACFDT) in the random-phase approximation (RPA). Like density functional theory, ACFDT is principally exact and offers fully first-principles derived operations. Expectably, this approach is much more demanding from a computational stance, making it very prohibitive, especially on larger systems.

A motivation was created to investigate whether another popular approach for tackling van der Waals dominated systems, the Grimme D2 dispersion corrections, might prove fit for van der Waals heterostructures. Being a semiempirical parametrization, it lacks the ab-initio nature of ACFDT-RPA. In return, it boasts almost negligible computational cost and has been proven to be surprisingly robust in a number of cases [41, 74, 85].

Looking back on what we learned in our discussion of results, we say that some justification for our proposition was found. Throughout, we deployed four different methods, namely simple LDA, GGA and each again with the addition of Grimme's corrections. Results were judged based on their coincidence with experiment where possible [58] and with analogous RPA findings elsewhere [1, 7]. This scheme was carried out for a wide range of quantities including relaxed configurational parameters, total energies as a function of interlayer spacing, Young's moduli and band gaps. While we found respectable agreement between LDA, GGA+D2 and RPA in some areas, GGA and LDA+D2 failed decidedly in every test and should not be considered worthwhile for further research on van der Waals heterostructures. We link this assessment to several observations:

- Early in our investigations of the total energy, we found GGA to predict a profound underbinding, implying that under ambient conditions graphene and hBN should be unable to cohere, rather than form a stable compound as demonstrated experimentally [80, 86].
- Exactly the opposite, LDA+D2 exhibited a severe overbinding, predicting minimum total energies as low as  $E_{0,\text{LDA+D2}} = -252 \text{ meV}$  per unit cell for some parts of the graphene-hBN moiré pattern. This is unrealistic when compared to RPA data of  $E_{0,\text{RPA}} = -83 \text{ meV}$ . The

latter benefits from having yielded Young's moduli that were successfully compared with experiment [1, 58].

- We checked layer separation as predicted by GGA and LDA+D2 for different areas of the moiré structure. Our findings were unlikely equilibrium interlayer distances corresponding to the type of misbinding, meaning very large  $4.29 \text{ \AA} < d_{0,\text{GGA}} < 4.51 \text{ \AA}$  (5.2.2) and very short  $2.91 \text{ \AA} < d_{0,\text{LDA+D2}} < 3.13 \text{ \AA}$  (5.2.3). This compares to  $3.35 \text{ \AA} < d_{0,\text{RPA}} < 3.55 \text{ \AA}$  for RPA as obtained by ref. [1]. A number of other quantities were derived from the total energy curves, e.g. strain energetics, Young's moduli (5.3.1), and band gaps (5.4.1) all of which showed poor compliance with RPA data.

On the up side, judging by the standard of RPA, the quality of LDA and GGA+D2 predictions was significantly better in several instances. Firstly, we found equilibrium interlayer spacings in the range of  $3.23 \text{ \AA} < d_{0,\text{LDA}} < 3.50 \text{ \AA}$  and  $3.13 \text{ \AA} < d_{0,\text{GGA+D2}} < 3.35 \text{ \AA}$  which is on average 2.4% and 6.1% smaller than what RPA predicts. For many requirements, this constitutes sufficient accuracy.

We also found partial agreement with respect to the total energy. As a function of the interlayer distance, LDA, GGA+D2 and RPA energy curves displayed a similar shape. In our discussion of results, this was shown to lead to qualitative agreement on Young's moduli and band gaps, and to similar relative differences between configurations. In the case of LDA, it stands to reason, that this quality is merely due to favorable error cancellation (see related discussion on page 18). For GGA+D2 however, which has been clearly shown not to benefit from this effect due by looking at GGA's severe underbinding in fig. 5.8, we suggest it might indicate a conceptually correct description of graphene-hBN and perhaps van der Waals heterostructures in general. If indeed the case, this would mean that the generalized gradient approximation in the DFT framework with an added semiempirical dispersion correction is able to fully model the physical processes of a system with long-range correlation. The quantitative difference in energy to RPA then only stems from disproportionate accountance of different energy contributions, which could be fixed by adjusting D2's parameter set as discussed on page 43.

In conclusion, we firstly suggest to do exactly that; depending on the robustness of D2 corrections and their applicability on other van der Waals heterostructures besides just graphene-hBN, adapting D2 empirical parameters specifically for this type of system could have a huge impact. Secondly, with the ultimate aim of giving theory the tools it needs to fully understand the physical processes in these complex many-body systems, we call for one or both of the following:

1. the development of new (computationally) more effective methods, enabling the study of large many-body systems exhibiting long-range correlation and interaction effects, or
2. the advancement of graphene-based nanoelectronics which would override the computational barrier on such theories that already exist.

# Bibliography

- [1] B. Sachs et al. “Adhesion and electronic structure of graphene on hexagonal boron nitride substrates”. In: *Physical Review B* 84 (19 Nov. 2011), p. 195414.
- [2] K. Capelle. “A bird’s-eye view of density-functional theory”. In: *Brazilian Journal of Physics* 36.4A (2006), pp. 1318–1343.
- [3] K. S. Novoselov et al. “Electric Field Effect in Atomically Thin Carbon Films”. In: *Science* 306.5696 (Oct. 2004), pp. 666–669. eprint: <http://www.sciencemag.org/content/306/5696/666.full.pdf>.
- [4] A. A. Balandin et al. “Superior Thermal Conductivity of Single-Layer Graphene”. In: *Nano Letters* 8.3 (Feb. 20, 2008), pp. 902–907.
- [5] K. Bolotin et al. “Ultrahigh electron mobility in suspended graphene”. In: *Solid State Communications* 146.9–10 (June 2008), pp. 351–355.
- [6] C. Lee et al. “Measurement of the Elastic Properties and Intrinsic Strength of Monolayer Graphene”. In: *Science* 321.5887 (2008), pp. 385–388. eprint: <http://www.sciencemag.org/content/321/5887/385.full.pdf>.
- [7] B. Sachs. “Two-Dimensional Crystals for Novel Nanoelectronics”. English. PhD thesis. Von-Melle-Park 3, 20146 Hamburg: Universität Hamburg, 2014.
- [8] X. Duan. “Approaching Terahertz Graphene Transistors”. In: *ECS Transactions* 35.3 (2011), pp. 239–252. eprint: <http://ecst.ecsdl.org/content/35/3/239.full.pdf+html>.
- [9] G. Giovannetti et al. “Substrate-induced band gap in graphene on hexagonal boron nitride: Ab initio density functional calculations”. In: *Physical Review B* 76 (7 Aug. 2007), p. 073103.
- [10] J. Slawinska, I. Zasada, and Z. Klusek. “Energy gap tuning in graphene on hexagonal boron nitride bilayer system”. In: *Physical Review B* 81 (15 Apr. 2010), p. 155433.
- [11] S. Grimme. “Semiempirical GGA-type density functional constructed with a long-range dispersion correction”. In: *Journal of Computational Chemistry* 27.15 (Nov. 2006), pp. 1787–1799.
- [12] P. Dirac. *The Principles of Quantum Mechanics*. Igal Meirovich, 2012.
- [13] T. Sauer et al. *David Hilbert’s Lectures on the Foundations of Physics 1915-1927: Relativity, Quantum Theory and Epistemology*. Vol. 5. Springer, 2009.
- [14] J. Neumann. *Mathematische Grundlagen der Quantenmechanik*. Verlag von Julius Springer Berlin, 1932.
- [15] H. Weyl. *The theory of groups and quantum mechanics*. Courier Dover Publications, 1950.
- [16] B. Sachs. “Doping Effects and Work Function Engineering of Graphene”. PhD thesis. Hamburg. Univ., 2010.
- [17] P. Hohenberg and W. Kohn. “Inhomogeneous Electron Gas”. In: *Physical Review* 136 (3B Nov. 1964), B864–B871.
- [18] R. Martin. *Electronic Structure: Basic Theory and Practical Methods*. Cambridge University Press, 2004.
- [19] M. Levy and J. P. Perdew. “Hellmann-Feynman, virial, and scaling requisites for the exact universal density functionals. Shape of the correlation potential and diamagnetic susceptibility for atoms”. In: *Physical Review A* 32 (4 Oct. 1985), pp. 2010–2021.
- [20] W. Kohn and L. J. Sham. “Self-consistent equations including exchange and correlation effects”. In: *Physical Review* 140.4A (1965), A1133.
- [21] R. Nalewajski. *Perspectives in Electronic Structure Theory*. Springer, 2012.
- [22] D. R. Hamann, M. Schlüter, and C. Chiang. “Norm-Conserving Pseudopotentials”. In: *Physical Review Letters* 43 (20 Nov. 1979), pp. 1494–1497.
- [23] G. B. Bachelet, D. R. Hamann, and M. Schlüter. “Pseudopotentials that work: From H to Pu”. In: *Physical Review Letters* 26 (8 Oct. 1982), pp. 4199–4228.

- [24] Wikipedia. *Pseudopotential*. Wikipedia - The Free Encyclopedia. 2014. URL: <http://en.wikipedia.org/w/index.php?title=Pseudopotential&oldid=619209548> (visited on 09/18/2014).
- [25] P. E. Blöchl. “Projector augmented-wave method”. In: *Physical Review B* 50 (24 Dec. 1994), pp. 17953–17979.
- [26] W. Kohn. “Nobel Lecture: Electronic structure of matter-wave functions and density functionals”. In: *Reviews of Modern Physics* 71.5 (1999), pp. 1253–1266.
- [27] R. G. Parr and W. Yang. *Density-functional theory of atoms and molecules*. Vol. 16. Oxford university press, 1989.
- [28] J. Tao et al. “Climbing the Density Functional Ladder: Nonempirical Meta-Generalized Gradient Approximation Designed for Molecules and Solids”. In: *Physical Review Letters* 91 (14 Sept. 2003), p. 146401.
- [29] D. M. Ceperley and B. J. Alder. “Ground State of the Electron Gas by a Stochastic Method”. In: *Physical Review Letters* 45 (7 Aug. 1980), pp. 566–569.
- [30] E. Engel et al. “Asymptotic properties of the exchange energy density and the exchange potential of finite systems: relevance for generalized gradient approximations”. In: *Zeitschrift für Physik D Atoms, Molecules and Clusters* 23.1 (1992), pp. 7–14.
- [31] J. P. Perdew, K. Burke, and M. Ernzerhof. “Generalized Gradient Approximation made simple”. In: *Physical Review Letters* 77 (18 Oct. 1996), pp. 3865–3868.
- [32] C. Filippi, C. J. Umrigar, and M. Taut. “Comparison of exact and approximate density functionals for an exactly soluble model”. In: *The Journal of Chemical Physics* 100.2 (Dec. 1994), pp. 1290–1296.
- [33] J. P. Perdew and A. Zunger. “Self-interaction correction to density-functional approximations for many-electron systems”. In: *Physical Review B* 23 (10 May 1981), pp. 5048–5079.
- [34] J. P. Perdew and Y. Wang. “Pair-distribution function and its coupling-constant average for the spin-polarized electron gas”. In: *Physical Review B* 46 (20 Nov. 1992), pp. 12947–12954.
- [35] Y.-H. Kim et al. “Two-dimensional limit of exchange-correlation energy functional approximations”. In: *Physical Review B* 61 (8 Feb. 2000), pp. 5202–5211.
- [36] W. Kohn, Y. Meir, and D. E. Makarov. “van der Waals Energies in Density Functional Theory”. In: *Physical Review Letters* 80 (19 May 1998), pp. 4153–4156.
- [37] M. Lein, J. F. Dobson, and E. K. U. Gross. “Toward the description of van der Waals interactions within density functional theory”. In: *Journal of Computational Chemistry* 20.1 (Jan. 1999), pp. 12–22.
- [38] J. F. Dobson and B. P. Dinte. “Constraint Satisfaction in Local and Gradient Susceptibility Approximations: Application to a van der Waals Density Functional”. In: *Physical Review Letters* 76 (11 Mar. 1996), pp. 1780–1783.
- [39] Y. Andersson et al. “Density-functional account of van der Waals forces between parallel surfaces”. In: *Solid State Communications* 106.5 (May 1998), pp. 235–238.
- [40] E. R. Johnson and A. D. Becke. “A post-Hartree-Fock model of intermolecular interactions: inclusion of higher-order corrections”. In: *The Journal of chemical physics* 124.17 (May 2006), p. 174104.
- [41] T. Buko et al. “Improved Description of the Structure of Molecular and Layered Crystals: Ab Initio DFT Calculations with van der Waals Corrections”. In: *The Journal of Physical Chemistry A* 114.43 (Oct. 2010). PMID: 20923175, pp. 11814–11824. eprint: <http://dx.doi.org/10.1021/jp106469x>.
- [42] X. Wu et al. “Towards extending the applicability of density functional theory to weakly bound systems”. In: *The Journal of Chemical Physics* 115.19 (Nov. 2001), pp. 8748–8757.
- [43] J. F. Dobson et al. “Prediction of dispersion forces: Is there a problem?” In: *Australian journal of chemistry* 54.8 (Feb. 2002), pp. 513–527.
- [44] Q. Wu and W. Yang. “Empirical correction to density functional theory for van der Waals interactions”. In: *The Journal of Chemical Physics* 116.2 (Jan. 2002), pp. 515–524.

- [45] S. Grimme. “Accurate description of van der Waals complexes by density functional theory including empirical corrections”. In: *Journal of Computational Chemistry* 25.12 (Sept. 2004), pp. 1463–1473.
- [46] S. Grimme et al. “Density functional theory with dispersion corrections for supramolecular structures, aggregates, and complexes of (bio)organic molecules”. In: *Organic and Biomolecular Chemistry* 5 (5 Jan. 2007), pp. 741–758.
- [47] D. f. C. M. P. Faculty of Physics. *About VASP*. University of Vienna. 2014. URL: <http://www.vasp.at/index.php/about-vasp/59-about-vasp> (visited on 09/19/2014).
- [48] D. f. C. M. P. Faculty of Physics. *INCAR-file*. University of Vienna. 2014. URL: <http://cms.mpi.univie.ac.at/vasp/guide/node91.html> (visited on 09/20/2014).
- [49] D. f. C. M. P. Faculty of Physics. *KPOINTS-file*. University of Vienna. 2014. URL: [http://cms.mpi.univie.ac.at/vasp/vasp/KPOINTS\\_file.html](http://cms.mpi.univie.ac.at/vasp/vasp/KPOINTS_file.html) (visited on 09/20/2014).
- [50] D. f. C. M. P. Faculty of Physics. *POSCAR-file*. University of Vienna. 2014. URL: <http://cms.mpi.univie.ac.at/vasp/guide/node59.html> (visited on 09/20/2014).
- [51] D. f. C. M. P. Faculty of Physics. *POTCAR file*. University of Vienna. 2014. URL: [http://cms.mpi.univie.ac.at/vasp/vasp/POTCAR\\_file.html](http://cms.mpi.univie.ac.at/vasp/vasp/POTCAR_file.html) (visited on 09/20/2014).
- [52] R. Kundu. “Tight-Binding Parameters for Graphene”. In: *Modern Physics Letters B* 25.03 (Jan. 2011), pp. 163–173. eprint: <http://www.worldscientific.com/doi/pdf/10.1142/S0217984911025663>.
- [53] K. Watanabe, T. Taniguchi, and H. Kanda. “Direct-bandgap properties and evidence for ultraviolet lasing of hexagonal boron nitride single crystal”. In: *Nature Materials* 3.6 (June 2004), pp. 404–409.
- [54] W. Auwärter et al. “XPD and STM investigation of hexagonal boron nitride on Ni(111)”. In: *Surface Science* 429.1–3 (June 1999), pp. 229–236.
- [55] R. S. Pease. “An X-ray study of boron nitride”. In: *Acta Crystallographica* 5.3 (May 1952), pp. 356–361.
- [56] Y. X. Zhao and I. L. Spain. “X-ray diffraction data for graphite to 20 GPa”. In: *Physical Review B* 40 (2 July 1989), pp. 993–997.
- [57] M. Katsnelson, K. Novoselov, and A. Geim. “Chiral tunnelling and the Klein paradox in graphene”. In: *Nature Physics* 2.9 (Aug. 2006), pp. 620–625.
- [58] C. R. Woods et al. “Commensurate-incommensurate transition in graphene on hexagonal boron nitride”. In: *Nature Physics* 10.6 (June 2014). Article, pp. 451–456.
- [59] A. K. Geim and K. S. Novoselov. “The rise of graphene”. In: *Nature Materials* 6.3 (Mar. 2007), pp. 183–191.
- [60] J. Xue et al. “Scanning tunnelling microscopy and spectroscopy of ultra-flat graphene on hexagonal boron nitride”. In: *Nature Materials* 10.4 (Feb. 13, 2011), pp. 282–285.
- [61] R. Decker et al. “Local Electronic Properties of Graphene on a BN Substrate via Scanning Tunneling Microscopy”. In: *Nano Letters* 11.6 (May 9, 2011), pp. 2291–2295.
- [62] D. f. C. M. P. Faculty of Physics. *EDIFF-tag*. University of Vienna. 2014. URL: <http://cms.mpi.univie.ac.at/vasp/guide/node105.html> (visited on 09/10/2014).
- [63] B. Sachs. personal communication. email. University of Hamburg, Sept. 10, 2014.
- [64] J. Harl and G. Kresse. “Accurate Bulk Properties from Approximate Many-Body Techniques”. In: *Physical Review Letters* 103 (5 July 2009), p. 056401.
- [65] A. Marini, P. García-González, and A. Rubio. “First-Principles Description of Correlation Effects in Layered Materials”. In: *Physical Review Letters* 96 (13 Apr. 2006), p. 136404.
- [66] J. F. Dobson, A. White, and A. Rubio. “Asymptotics of the Dispersion Interaction: Analytic Benchmarks for van der Waals Energy Functionals”. In: *Physical Review Letters* 96 (7 Feb. 2006), p. 073201.
- [67] H. Rydberg et al. “Van der Waals Density Functional for Layered Structures”. In: *Physical Review Letters* 91 (12 Sept. 2003), p. 126402.
- [68] J. P. Perdew and K. Burke. “Comparison shopping for a gradient-corrected density functional”. In: *International Journal of Quantum Chemistry* 57.3 (Feb. 1996), pp. 309–319.

- [69] D. f. C. M. P. Faculty of Physics. *DFT-D2 method of Grimme*. University of Vienna. 2014. URL: [http://cms.mpi.univie.ac.at/vasp/vasp/DFT\\_D2\\_method\\_Grimme.html](http://cms.mpi.univie.ac.at/vasp/vasp/DFT_D2_method_Grimme.html) (visited on 09/23/2014).
- [70] Wikipedia. *Young's modulus*. Wikipedia - The Free Encyclopedia. Sept. 16, 2014. URL: [http://en.wikipedia.org/w/index.php?title=Young's\\_modulus&oldid=625853216](http://en.wikipedia.org/w/index.php?title=Young's_modulus&oldid=625853216) (visited on 09/25/2014).
- [71] E. Merritt. *Fit*. Gnuplot. Mar. 3, 2007. URL: [http://gnuplot.sourceforge.net/docs\\_4.2/node82.html](http://gnuplot.sourceforge.net/docs_4.2/node82.html) (visited on 09/25/2014).
- [72] Wikipedia. *Levenberg–Marquardt algorithm*. Wikipedia - The Free Encyclopedia. July 21, 2014. URL: [http://en.wikipedia.org/wiki/Levenberg%26Marquardt\\_algorithm](http://en.wikipedia.org/wiki/Levenberg%26Marquardt_algorithm) (visited on 09/25/2014).
- [73] K. H. Michel and B. Verberck. “Theory of the elastic constants of graphite and graphene”. In: *Physica Status Solidi (b)* 245.10 (Oct. 2008), pp. 2177–2180.
- [74] P. Jinwoo, D. Y. Byung, and H. Suklyun. “Ab initio Calculations with van der Waals Corrections: Benzene-benzene Intermolecular Case and Graphite”. In: *Journal of the Korean Physical Society* 59 (2011), p. 196.
- [75] P. Rinke et al. “Image States in Metal Clusters”. In: *Physical Review A* 70 (6 Dec. 2004), p. 063201.
- [76] S. Lebegue et al. “Cohesive Properties and Asymptotics of the Dispersion Interaction in Graphite by the Random Phase Approximation”. In: *Physical Review Letters* 105 (19 Nov. 2010), p. 196401.
- [77] A. Crespo et al. “A DFT-Based QM-MM Approach Designed for the Treatment of Large Molecular Systems: Application to Chorismate Mutase”. In: *Journal of Physical Chemistry B* 107.49 (Nov. 15, 2003), pp. 13728–13736.
- [78] C. Tuma and J. Sauer. “Treating dispersion effects in extended systems by hybrid MP2:DFT calculations—protonation of isobutene in zeolite ferrierite”. In: *Physical Chemistry Chemical Physics* 8.34 (July 2006), pp. 3955–3965.
- [79] J. Jensen. *Molecular Modeling Basics: DFT-D, DFT-D2 and DFT-D3: Density functional dispersion correction*. Mar. 23, 2013. URL: <http://molecularmodelingbasics.blogspot.de/2013/03/dft-d-dft-d2-and-dft-d3-density.html> (visited on 09/27/2014).
- [80] A. Geim and I. Grigorieva. “Van der Waals heterostructures”. In: *Nature* 499.7459 (2013), pp. 419–425.
- [81] C. Cress et al. “Total Ionizing Dose Induced Charge Carrier Scattering in Graphene Devices”. In: *Nuclear Science, IEEE Transactions on* 59.6 (Dec. 2012), pp. 3045–3053.
- [82] T. Cao et al. “Valley-selective circular dichroism of monolayer molybdenum disulphide”. In: *Nature Communications* 3 (June 6, 2012), pp. 887+.
- [83] J. Harl and G. Kresse. “Cohesive energy curves for noble gas solids calculated by adiabatic connection fluctuation-dissipation theory”. In: *Physical Review B* 77 (4 Jan. 2008), p. 045136.
- [84] D. Lu et al. “Ab initio”. In: *Physical Review Letters* 102 (20 May 2009), p. 206411.
- [85] T. Kerber, M. Sierka, and J. Sauer. “Application of semiempirical long-range dispersion corrections to periodic systems in density functional theory”. In: *Journal of Computational Chemistry* 29.13 (Oct. 2008), pp. 2088–2097.
- [86] T. O. Wehling, A. I. Lichtenstein, and M. I. Katsnelson. “First-principles studies of water adsorption on graphene: The role of the substrate”. In: *Applied Physics Letters* 93.20 (Nov. 2008), pp. 1–3.

## Acknowledgements

Thanks go out to all the people who helped me in some way or another during the time I spent on this thesis. I wish to mention my academic advisor Burkhard Sachs who was very patient with me, and ever on the scene, when I needed more explaining or further input. I feel like I still owe him some potato dumplings. Secondly, to my good friend Lars Hansen who would drop

whatever he was doing and help me time and again when I faced a frustrating scripting problem, be it with a shell, perl or awk script, or some regular expression that wouldn't work. Lars, you saved me many hours of fruitless trial and error. Thirdly, to Michael Vedmedenko, who could always spare a moment (or a while) for me and did a tremendous job in IT support, knowing the best solution and quickest fix whenever some integral part of my work environment quit functioning. I could not have completed this project in such a timeframe without his help. And last but certainly not least to my family, who supported me in all other areas of life.

## Declaration of Authorship

Hiermit bestätige ich, dass die vorliegende Arbeit von mir selbständig verfasst wurde und ich keine anderen als die angegebenen Hilfsmittel – insbesondere keine im Quellenverzeichnis nicht benannten Quellen benutzt habe und die Arbeit von mir vorher nicht einem anderen Prüfungsverfahren eingereicht wurde. Die eingereichte schriftliche Fassung entspricht der auf dem elektronischen Speichermedium. Ich bin damit einverstanden, dass die Bachelorarbeit veröffentlicht wird.

Hamburg, 16.10.2014

---

Janosh Riebesell